

An integrated approach for monitoring structural deformation of aquaculture net cages

Biao Su^{a,*}, Eleni Kelasidi^a, Kevin Frank^a, Joakim Haugen^a, Martin Føre^b, Magnus Oshaug Pedersen^a

^a Department of Seafood Technology, SINTEF Ocean, Trondheim, Norway

^b Department of Engineering Cybernetics, NTNU, Trondheim, Norway

ARTICLE INFO

Keywords:

Aquaculture net cages
Real-time monitoring
Numerical model
Acoustic positioning system

ABSTRACT

The majority of present marine finfish production is conducted in flexible net cages which can deform when they are subjected to water movements generated by currents. The ability to monitor net deformation is important for performing cage operations and evaluation of fish health and welfare under changing environment. This paper presents a new method for real-time monitoring of net cage deformations that is based on an integrated approach where positioning sensor data is incorporated into a numerical model. An underwater positioning system was deployed at a full-scale fish farm site, with three acoustic sensors mounted on a cage measuring positions of the net at different depths. A novel numerical model with an adaptive current field was used to simulate net cage deformations, where the magnitude and direction of the current could be adapted by continuously assessing deviations between the simulated and the measured positions of the net. This method was found to accurately predict the pre-defined current velocity profiles in a set of simulated experiments. In the field experiment, a good agreement was also obtained between the simulated positions of the net and the acoustic sensor data. The integrated approach was shown to be well suited for in-situ real-time monitoring of net cage deformations by using a significantly reduced number of sensors.

1. Introduction

Atlantic salmon (*Salmo salar*) is currently one of the most significant farmed finfish species in marine aquaculture. The majority of the salmon production cycle is conducted in flexible net cages that are placed in floating fish farms moored to the seabed or the shore (see e.g. in Fig. 1). These cages can deform when subjected to water movements generated by currents, altering the available volume for the fish and influencing cage management and operations. The loss of cage volume has been shown to affect fish growth and mortality rates due to reduced oxygen flow and increased stress levels in the fish, particularly when the stocking density is high (Turnbull et al., 2005). Water current in itself can also cause stress to the fish, as the fish have to swim faster and expend more energy to avoid contact with the net enclosure and other fish (Remen et al., 2016). Real-time detection of net deformation could act as a useful “early warning” system for fish farm operators to prevent uncontrolled reduction of cage volume (Lader et al., 2008). The ability to monitor net deformation is also essential for the automation of

inspection, maintenance and repair operations in fish farms. This harmonises with the Precision Fish Farming (PFF) concept which outlines how innovative technologies and automation principles may be used to improve the ability to monitor, control and document aquaculture productions (Føre et al., 2018).

The deformation of net cages in current and waves has been extensively studied by means of numerical modelling (e.g. Aarsnes et al., 1990; Lader et al., 2003; Tsukrov et al., 2003; Fredheim, 2005; Huang et al., 2007; Zhao et al., 2007; Berstad et al., 2014; Endresen et al., 2014; Moe-Føre et al., 2016; Shen, 2018) and model testing (e.g. Lader and Enerhaug, 2005; Huang et al., 2006; Kristiansen and Faltinsen, 2015). The current and wave forces acting on a net structure are typically calculated by using Morison-type approach and experimentally based screen models (Løland, 1991; Kristiansen and Faltinsen, 2012). Due to the detailed and flexible geometry of the net consisting of millions of slender twines, a complete fluid–structure interaction analysis is not feasible today. A more common practice for modelling the interaction between current and cage is to consider the net as a porous medium (e.g.

* Corresponding author. SINTEF Ocean, Department of Seafood Technology, Trondheim, Norway .

E-mail address: biao.su@sintef.no (B. Su).



Fig. 1. An example of large Norwegian fish farm with 15 flexible net cages. Each net cage can have a volume of up to $50,000 \text{ m}^3$ and hold up to 200,000 farmed Atlantic salmons.

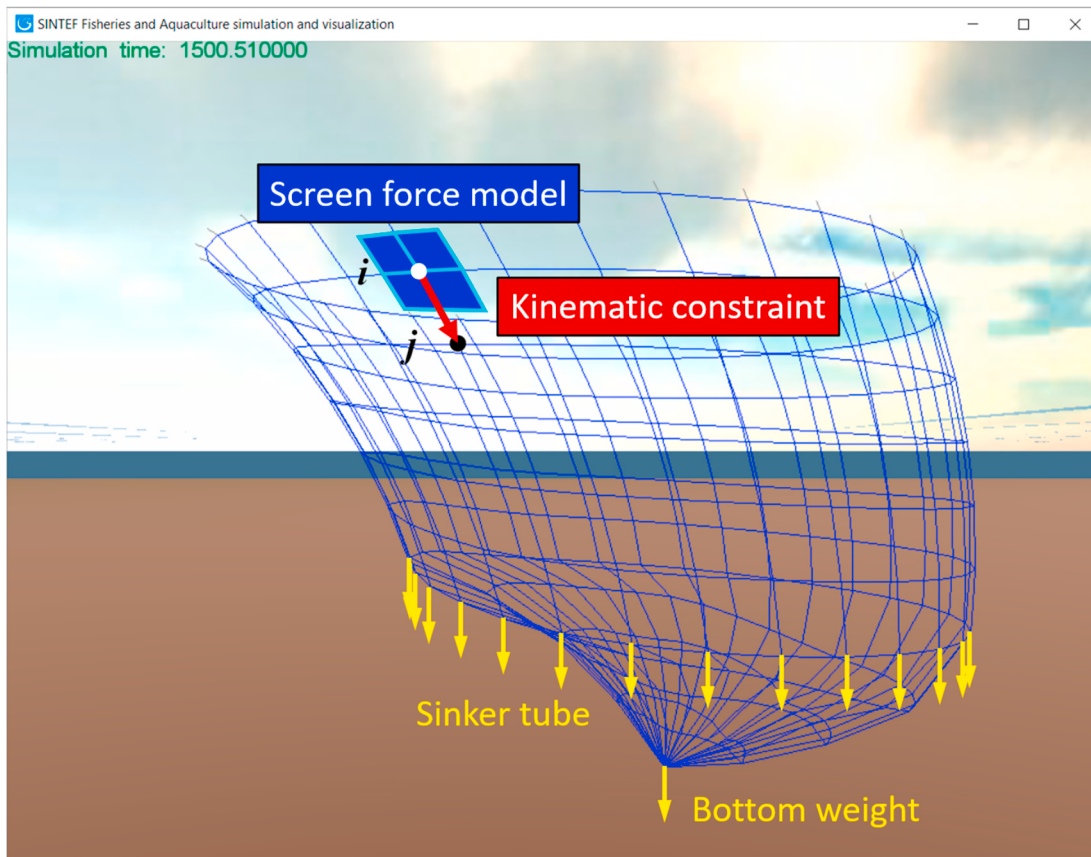


Fig. 2. Simplified net cage model. The netting structure is divided into interconnected truss elements by keeping a constant solidity ratio across elements. The red arrow denotes the kinematic constraint added to a given node considering the axial stiffness of one truss element. The shaded blue areas represent the net panels surrounding a given node and are used to calculate the hydrodynamic forces (screen force model). The top of the cage is fixed or connected to a floating collar. A sinker tube and a bottom weight can be connected to the net or simplified as vertical forces applied on the corresponding net nodes. (For interpretation of the references to colour in this figure legend, the reader is referred to the Web version of this article.)

Zhao et al., 2013; Bi et al., 2014; Yao et al., 2016). Although computational requirements in such simulations may be reduced by not resolving or simplifying the representation of the resulting fluid flow around the net, the simulation model of a full-scale net cage considering the influence on or from the fish (e.g. Filgueira et al., 2017; Tang et al., 2017) can still be computationally intensive for real-time implementations.

Full-scale field measurements of net cage deformations are challenging. The ones that exist have used pressure (depth) tags (Lader et al., 2008; Klebert et al., 2015) and acoustic sensor data (DeCew et al., 2013) to estimate cage volumes under various current conditions. By using positioning sensors mounted on the cage at several depths, these studies achieved good approximations of cage volume, but relied on a considerable number of sensors and were not used for real-time monitoring.

Furthermore, the volume approximation techniques could not provide detailed information about the deformed net geometry that can be used for operational tasks, such as autonomous net inspection operations, for which it is essential to instantaneously track the travelled path of an underwater vehicle relative to a net pen (Rundtop and Frank, 2016; Arnesen et al., 2018).

In this study, a real-time numerical model was developed for the simulation and monitoring of net cage deformations. Positioning data obtained from three acoustic sensors mounted on a full-scale net cage were incorporated into the numerical model by continuously altering and adapting the magnitude and direction of the current used in the simulation, dependent on differences between the simulated and the measured positions of the net. This method was implemented as a part of

a general control framework for autonomous operations in fish farms that considers interactions with fish and flexible structures (Su et al., 2019). In addition to the deformed net geometry, the integrated approach was able to provide estimated values of the current as inputs for the evaluation of environmental disturbances to the fish and autonomous navigation (Kelasidi et al., 2017).

2. Materials and methods

The proposed approach for the monitoring of net cage deformation is implemented in a software framework, FhSim, which allows a high degree of flexibility to combine different mathematical models, numerical solvers and estimation techniques for time-domain representation of a complex system (Reite et al., 2014; Su et al., 2019). In the following, the numerical simulation model of net cage, the underwater positioning system and the integrated approach for cage monitoring are introduced, respectively.

2.1. Numerical simulation model

Because the number of net twines for a net cage is typically in the order of 10 million, complete structural modelling is not feasible in a model designed for real-time applications. Fig. 2 shows a simplified model of net cage structure which is set up with a netting material (knotless with square meshes and negligible bending stiffness) that is widely used in the aquaculture industry. Equivalent truss elements with only axial stiffness are used by keeping the same solidity ratio (S_n , defined as the ratio of the projected netting material area to the total area of a net panel) as the selected netting material across all elements. A typical net cage system also consists of a floating collar, a sinker tube, weights and various mooring components. The corresponding simulation models in FhSim have been described in detail by Endresen et al. (2014), along with a more sophisticated structural model for the net than that is used in the present study. The simplified net model can be connected to other existing models (e.g. floating collar and sinker tube) in FhSim for the simulation of a complete net cage system. To save simulation time, it may be assumed that the net is fixed on the top, while the sinker tube and bottom weight can be simplified by applying equivalent forces on the corresponding net nodes (see in Fig. 2).

2.1.1. Equations of motion for the net node

The deformation of the net cage structure is modelled by solving the equations of motion for each net node (as shown in Fig. 2) constrained by the interconnected truss elements and under the effect of hydrodynamic forces:

$$m_i \ddot{\mathbf{x}}_i = \sum_{n=1}^{N_T} \mathbf{K}_n + \sum_{n=1}^{N_p} (\mathbf{F}_n + \mathbf{A}_n) \quad (1)$$

where m_i is the local mass of the net represented by node i , $\dot{\mathbf{x}}_i \in \mathbb{R}^3$ (three-dimensional vector) is the acceleration vector of the node, N_T is the number of trusses connected with the node, $\mathbf{K}_n \in \mathbb{R}^3$ is the constraint force from one of the trusses, N_p is the number of net panels surrounding the node, $\mathbf{F}_n \in \mathbb{R}^3$ is the sum of drag and lift forces on one of the net panels, $\mathbf{A}_n \in \mathbb{R}^3$ is the corresponding added mass force, and as a first approximation, $\sum_{n=1}^{N_p} \mathbf{A}_n \approx -m_i(\rho_w / \rho_n) \ddot{\mathbf{x}}_i$ (Shen, 2018), where ρ_w is the water density and ρ_n is the density of the netting material.

2.1.2. Kinematic constraints for the truss element

A truss element connecting node i and node j is characterized by a vector $\mathbf{t}_{ij} \in \mathbb{R}^3$, that is defined as

$$\mathbf{t}_{ij} = \mathbf{x}_j - \mathbf{x}_i \quad (2)$$

where $\mathbf{x}_j \in \mathbb{R}^3$ is the position vector of node j , and $\mathbf{x}_i \in \mathbb{R}^3$ is the position vector

of node i . The quadratic constraint for the truss length, l_{ij} , is written as

$$C_{ij} = |\mathbf{t}_{ij}|^2 - l_{ij}^2 \quad (3)$$

Based on the Baumgarte stabilization method described in Johansen (2007), the quadratic constraint, C_{ij} , can be incorporated into the equations of motion of the node (Eq. (1)) as the constraint force

$$\mathbf{K}_{ij} = \frac{\mathbf{t}_{ij}}{|\mathbf{t}_{ij}|} \left(k_{pl} C_{ij} + k_{dl} \dot{C}_{ij} \right) \quad (4)$$

where $k_{pl} > 0$ and $k_{dl} > 0$ are the specified control gains. In addition, the quadratic constraint may be simplified by using the feedback linearization technique as described in Johansen (2007)

$$\mathbf{K}_{ij} = \frac{\mathbf{t}_{ij}}{|\mathbf{t}_{ij}|} \left(k_{pl} (|\mathbf{t}_{ij}| - l_{ij}) + k_{dl} \left(\frac{\mathbf{t}_{ij}^\top \mathbf{t}_{ij}}{|\mathbf{t}_{ij}|} - l_{ij} \right) \right) \quad (5)$$

with this simplification, the axial dynamics of the truss element can be adjusted to maintain its natural frequencies by choosing k_{pl} in accordance to

$$k_{pl} = \frac{E_{ij} A_{ij}}{l_{ij}} \quad (6)$$

where E_{ij} is the elastic modulus of the netting material, and A_{ij} is the equivalent cross-sectional area of the truss element. For modelling and simulation of slender elastic structures, the stability requirement is often related to the Courant number defined as

$$\gamma = \max_i \frac{w_i \Delta t}{l_i} \leq 1 \quad (7)$$

where l_i is the length of element i , w_i is the material wave speed of the element, and Δt is the integrator time step of the simulation. For $\gamma = 1$, the critical time step may be found as

$$\Delta t_c = \min_i \frac{l_i}{w_i} \quad (8)$$

Considering a typical netting material (e.g. elastic modulus: $E = 1.0$ GPa; density: $\rho = 1040$ kg/m) used in the aquaculture industry, the axial wave speed of a net twine can be approximated by

$$w_i = \sqrt{\frac{E_i}{\rho_i}} \approx \sqrt{\frac{10^9 \text{ Pa}}{10^3 \text{ kg/m}^3}} = 10^3 \text{ m/s} \quad (9)$$

This indicates that if the minimum element length is in the order of 1 m (which is common practice), the critical time step would be in the order of 10^{-3} s. Reducing the element length (i.e. mesh refinement) would require a smaller time step, which is a well-known numerical challenge when considering performance versus fidelity for such simulations.

Implicit time integration methods are usually used to solve such problems. Although the criterion defined by Eq. (8) may be relaxed for some implicit solvers, the computational time would still be a problem because of the iterative nature of such approaches. To reduce the Courant number, the control gains k_{pl} and k_{dl} in Eq. (4) and Eq. (5) may be chosen to appropriate values according to the integrator time step (Johansen, 2007). By doing this, the elastic modes of the truss elements will be exchanged by the kinematic constraints which provide the desired structural properties (e.g. the tensions of all the truss elements). In the present study, the high-frequency axial dynamics of each truss element are filtered out based on the Baumgarte stabilization method, since it is the transversal dynamics which dominate net deformations, and a steady state of net configuration is of interest.

2.1.3. Hydrodynamic model

The experimentally based screen type of force model proposed by

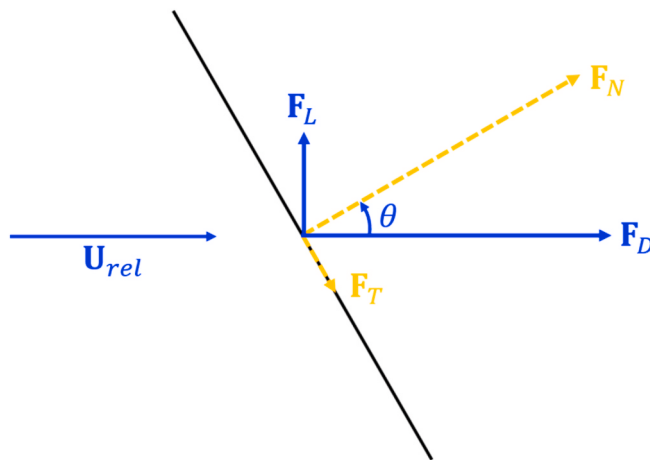


Fig. 3. Drag (\mathbf{F}_D) and lift (\mathbf{F}_L) forces on a net panel, where θ is the angle between the normal of the net panel and the direction of the instantaneous, relative fluid velocity, \mathbf{U}_{rel} . \mathbf{F}_N and \mathbf{F}_T denote the corresponding normal and tangential components of the hydrodynamic, viscous forces.

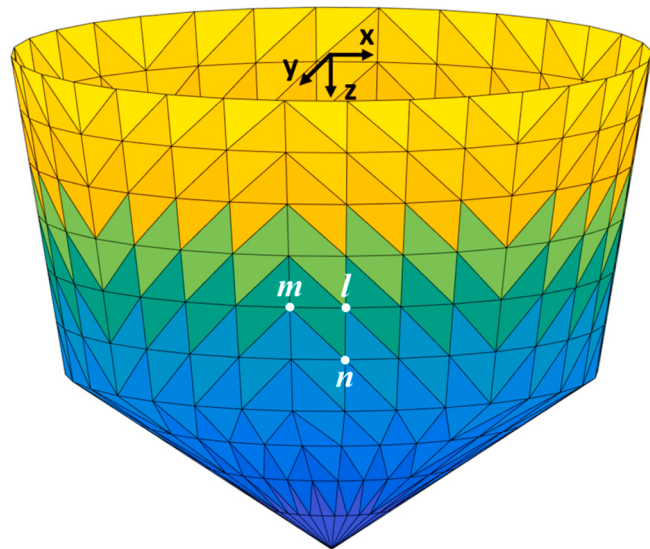


Fig. 4. Netting structure represented by a closed manifold triangular surface for volume calculation.

Kristiansen and Faltinsen (2012) is used to calculate the hydrodynamic, viscous forces acting on the net. The screen force model was originally developed for steady flow, and it was shown to give clear improvements in calculating the drag and lift forces on the net cages in current as compared with a Morison type of force model (Cheng et al., 2020). Considering the high Keulegan-Carpenter number with respect to the twine diameter, the flow in waves can be assumed as quasi-steady, thus the screen force model is considered to be also applicable in waves (Kristiansen and Faltinsen, 2015).

The screen force model divides the netting structure into a number of flat net panels, or screens (as shown in Fig. 2). Each net panel is assumed to experience a viscous normal force, $\mathbf{F}_N \in \mathbb{R}^3$, due to a pressure drop proportional to the square of the instantaneous, relative fluid velocity, $\mathbf{U}_{rel} \in \mathbb{R}^3$, and a tangential force, $\mathbf{F}_T \in \mathbb{R}^3$, due to the flow deflection by the net twines. The resultant force can be, alternatively, decomposed into the drag force, $\mathbf{F}_D \in \mathbb{R}^3$, and the lift force, $\mathbf{F}_L \in \mathbb{R}^3$, as shown in Fig. 3. The non-dimensional drag and lift force coefficients are defined as

$$C_D = \frac{|\mathbf{F}_D|}{0.5\rho_w A |\mathbf{U}_{rel}|^2} \quad (10)$$

$$C_L = \frac{|\mathbf{F}_L|}{0.5\rho_w A |\mathbf{U}_{rel}|^2} \quad (11)$$

where ρ_w is the water density and A is the panel area. The instantaneous, relative fluid velocity, \mathbf{U}_{rel} is defined as

$$\mathbf{U}_{rel} = r\mathbf{U}_\infty + \mathbf{U}_w - \dot{\mathbf{x}}_i \quad (12)$$

where $\mathbf{U}_\infty \in \mathbb{R}^3$ is the incoming current velocity, r is the velocity reduction (wake) factor, $\mathbf{U}_w \in \mathbb{R}^3$ is the incident wave particle velocity at the position of the node and $\dot{\mathbf{x}}_i \in \mathbb{R}^3$ is the velocity of node i . The practical importance of the velocity reduction is that the rear part of the cage will experience a reduced inflow, as described in Løland (1991):

$$r = 1 - 0.46c_d \quad (13)$$

where c_d is the calculated drag coefficient for a vertical net panel. The wake effect for the oscillatory flow is difficult to be incorporated, thus it is often assumed that only the steady part of the flow, i.e. the current, is reduced (Shen, 2018).

Kristiansen and Faltinsen (2012) used the experimental data from Goldstein (1965) to represent the drag coefficient of a circular cylinder, $C_D^{cir.cyl}$, as a seventh order polynomial of $\log_{10} Rn$ for the Reynolds number range $10^{3/2} \leq Rn \leq 10^4$,

$$C_D^{cir.cyl} = -78.46675 + 254.73873(\log_{10} Rn) - 327.8864(\log_{10} Rn)^2 + 223.64577(\log_{10} Rn)^3 - 87.92234(\log_{10} Rn)^4 + 20.00769(\log_{10} Rn)^5 - 2.44894(\log_{10} Rn)^6 + 0.12479(\log_{10} Rn)^7 \quad (14)$$

For a flat net panel, the Reynolds number is defined as

$$Rn = \frac{|\mathbf{U}_{rel}| d_w}{\nu(1 - Sn)} \quad (15)$$

where d_w is the net twine diameter and ν is the kinematic viscosity of water. The drag and lift coefficients may formally be represented by the Fourier series of θ , which is the angle between \mathbf{U}_{rel} and the normal of the net panel. One approximation is to keep the first two terms in each series, i.e.

$$C_D(\theta) = c_d(0.9 \cos \theta + 0.1 \cos 3\theta) \quad (16)$$

$$C_L(\theta) = c_l(1.0 \sin 2\theta + 0.1 \sin 4\theta) \quad (17)$$

where

$$c_d = C_D(0) = C_D^{cir.cyl} \frac{Sn(2 - Sn)}{2(1 - Sn)^2} \quad (18)$$

$$c_l = C_L(\pi/4) = \left(0.5c_d - \frac{2\pi c_d}{32 + 2c_d} \right) / \sqrt{2} \quad (19)$$

Eq. (16) to Eq. (19) relate the drag and lift coefficients of a net panel to the Reynolds number dependent drag coefficient of a circular cylinder, which are applicable for $10^{3/2} \leq Rn \leq 10^4$, $Sn \leq 0.5$ and $0 \leq \theta \leq \pi/2$. A thorough description of these formulations and the corresponding parametric studies can be found in Kristiansen and Faltinsen (2012).

2.1.4. Cage volume calculation

A generalized method based on Rohmer et al. (2009) is also implemented for the calculation of the enclosed volume of the net. Herein, the netting structure is represented by a closed manifold triangle surface, S , and its vertex positions are denoted by $\mathbf{p}_i = (x_i, y_i, z_i) \in \mathbb{R}^3$, $i = 1, \dots, N$. The

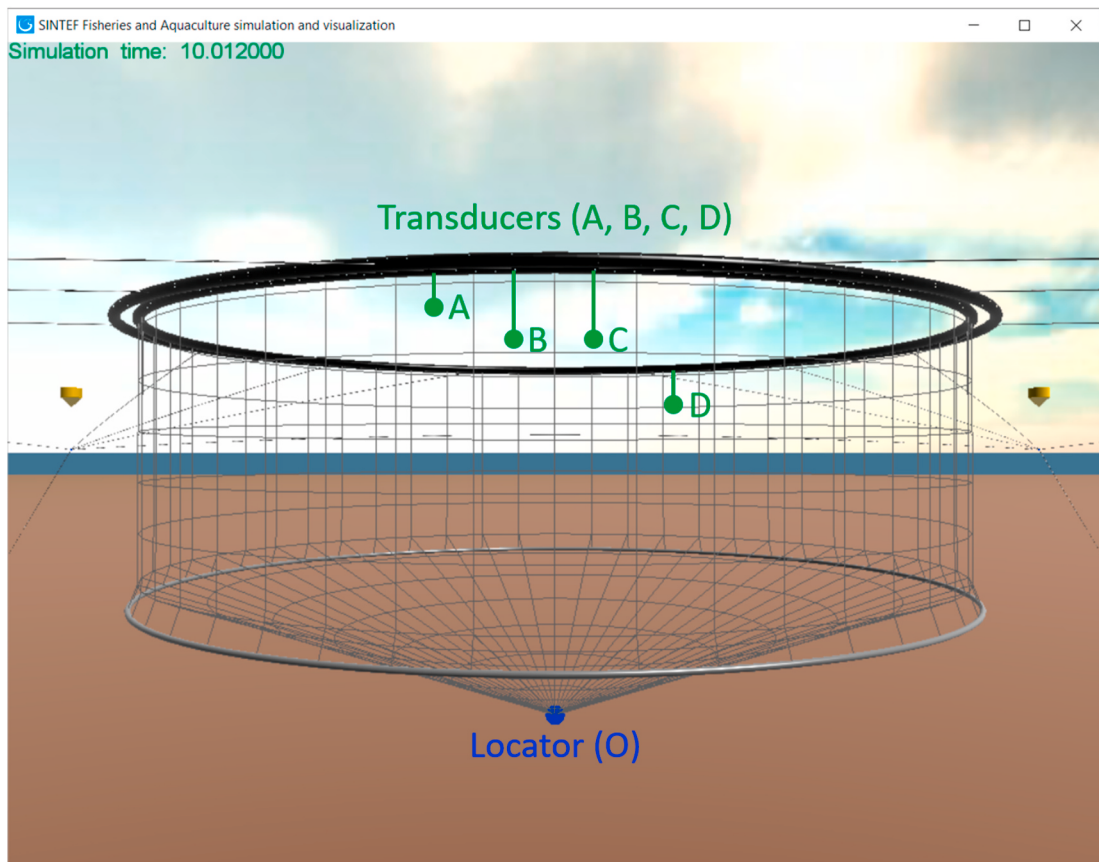


Fig. 5. SBL based positioning system for the use in aquaculture net cages.

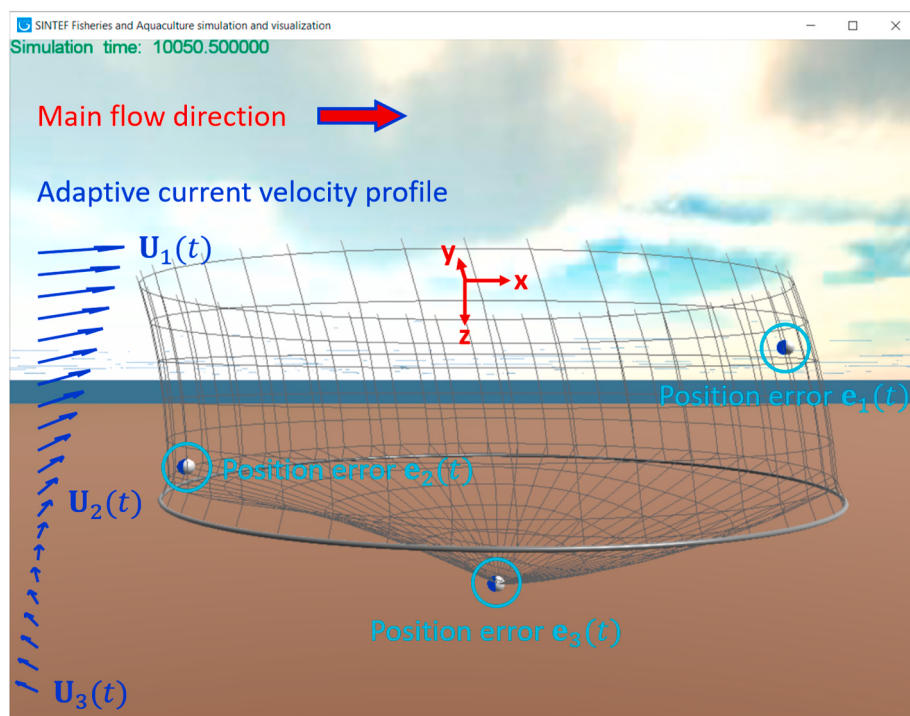


Fig. 6. Estimation of the incoming current velocity profile and the resulting cage deformations based on a set of measured positions of the net.

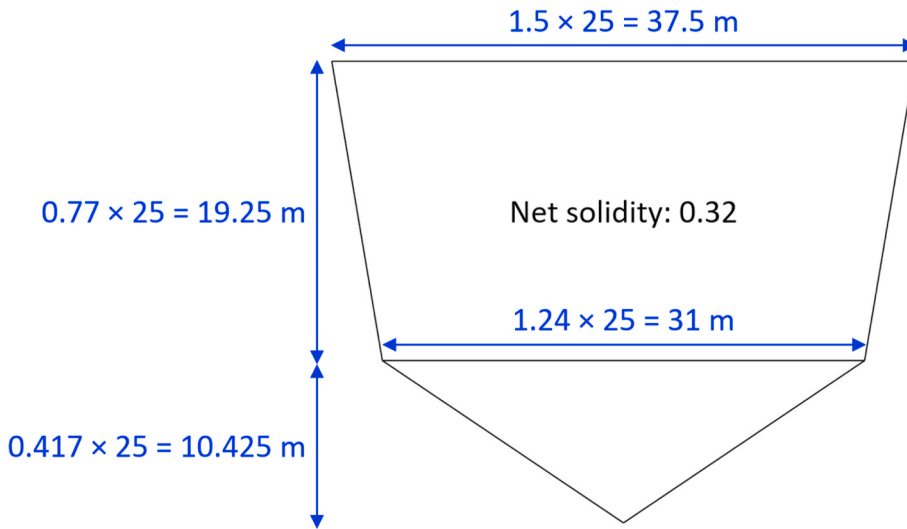


Fig. 7. Sketch of the net cage used in the model tests (He et al., 2018) and the up-scaled dimensions used in the simulations.

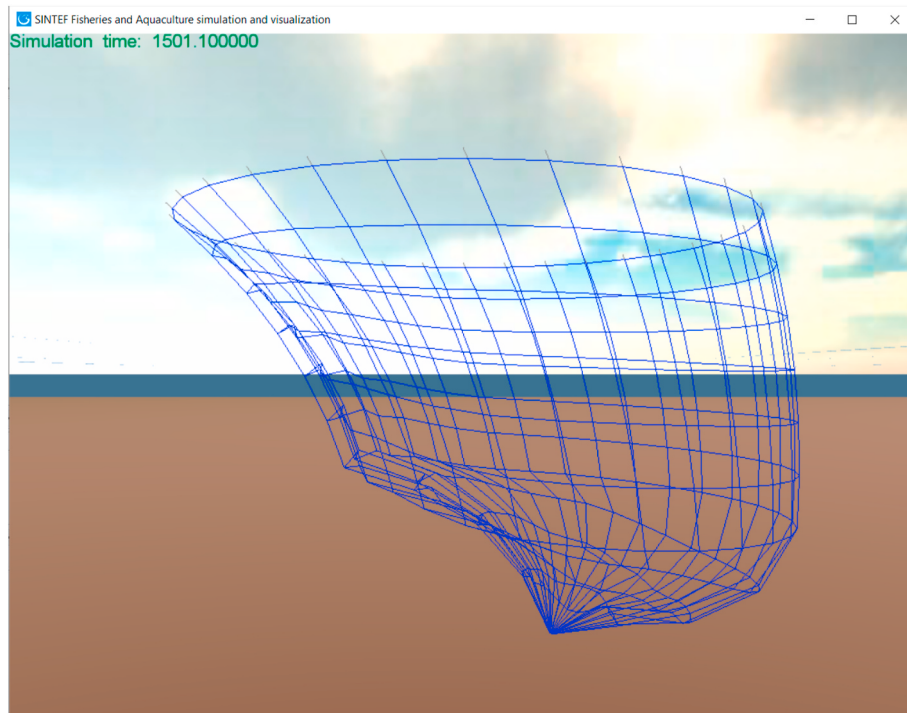


Fig. 8. Simulated steady-state shape of the cage in combined current ($U_\infty = 0.5 \text{ m/s}$) and waves ($H_s = 2 \text{ m}$; $T_p = 6 \text{ s}$).

enclosed volume of S is then given by

$$V = \sum_{\text{face}(l,m,n) \in S} \frac{z_l + z_m + z_n}{6} \begin{vmatrix} (x_m - x_l) & (y_m - y_l) \\ (x_n - x_l) & (y_n - y_l) \end{vmatrix} \quad (20)$$

where $\text{face}(l, m, n) = \Delta(\mathbf{p}_l, \mathbf{p}_m, \mathbf{p}_n)$ is a surface triangle of S . This trilinear expression, as described in Rohmer et al. (2009), corresponds to the sum of the signed volumes of the prisms spanned by the surface triangles and their projections onto the x-y plane (see Fig. 4).

2.2. Underwater positioning system

A short baseline (SBL) acoustic positioning system (Milne, 1983) determines the position of an underwater target by acoustically measuring the distance from a transponder (locator) mounted on the

tracked target to three or more baseline transducers (receiver) mounted on boats or ships that are either anchored or under way. While ultra-short baseline (USBL) systems offer a fixed accuracy, SBL positioning accuracy improves with transducer spacing. This means that an SBL system can achieve a precision and position stability similar to that of the sea floor mounted long baseline (LBL) system when there is sufficient space, making the system suitable for high-accuracy survey work.

In the present study, an SBL based positioning system was developed by Water Linked AS with instrument size and robustness being optimized for the use in aquaculture net cages. As shown in Fig. 5, four baseline transducers (A, B, C, D) are mounted on the floating collar and one locator (O) is mounted on the net. The baseline transducer (A) sends a signal, which is received by the locator. The locator replies, and the reply is received by the four transducers. The measurements of signal run time yield the distances O-A, O-B, O-C and O-D, which are used to

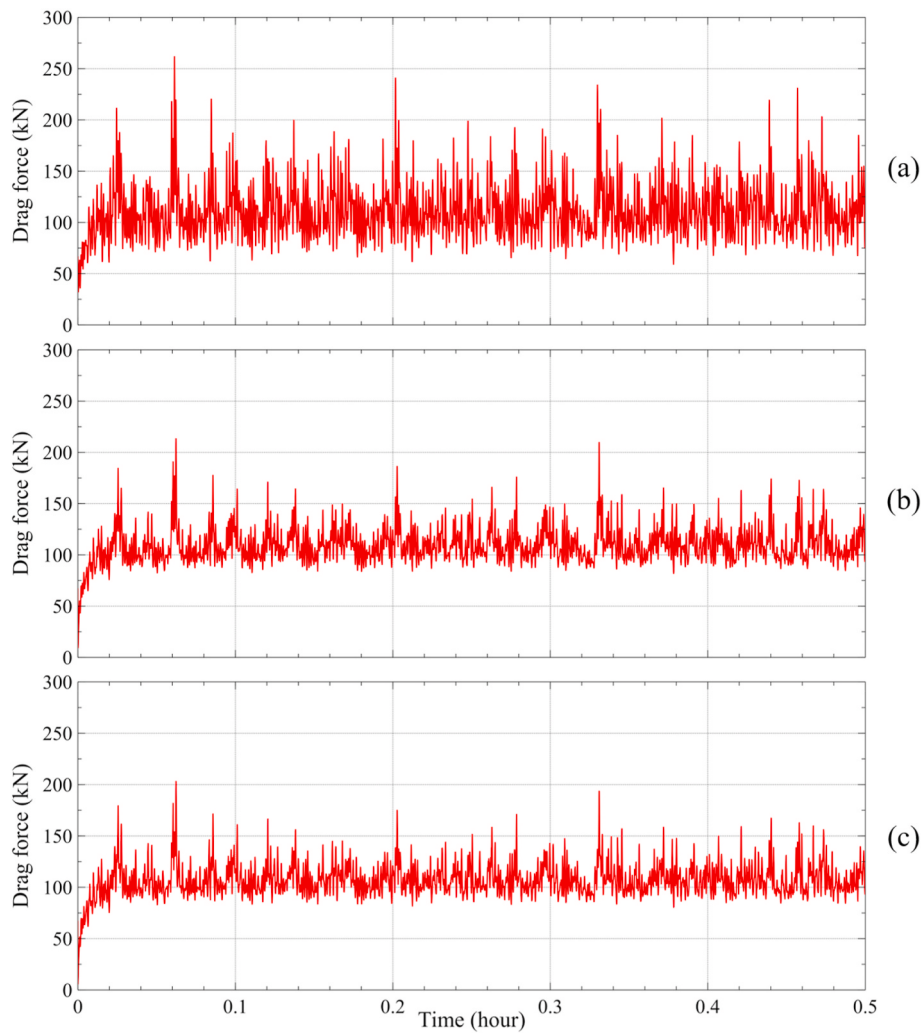


Fig. 9. Simulated time series of the total drag forces on the net: (a) $\Delta t = 0.1$ s, (b) $\Delta t = 0.01$ s, (c) $\Delta t = 0.001$ s.

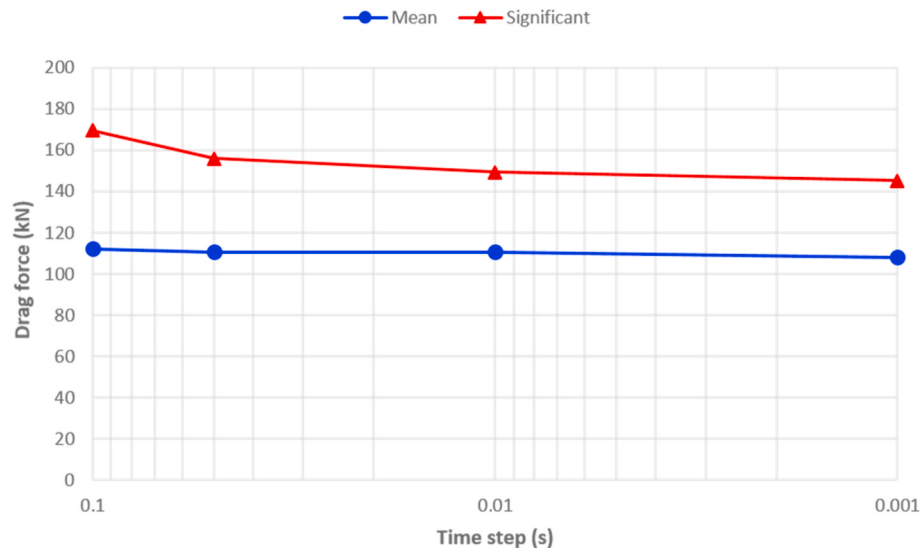


Fig. 10. Mean and significant values of the total drag forces on the net ($\Delta t = 0.001\text{--}0.1$ s).

calculate the position of the locator by triangulation or position search algorithms. The resulting target positions are relative to the location of the baseline transducers and can thus be converted to a cage-referenced coordinate system which is fixed to the floating collar.

The acoustic signals may be subjected to scattering and damping due to the swimming fish, rendering real-time communications with good coverage throughout the entire cage challenging to achieve. Water Linked AS have therefore developed specialized signal processing

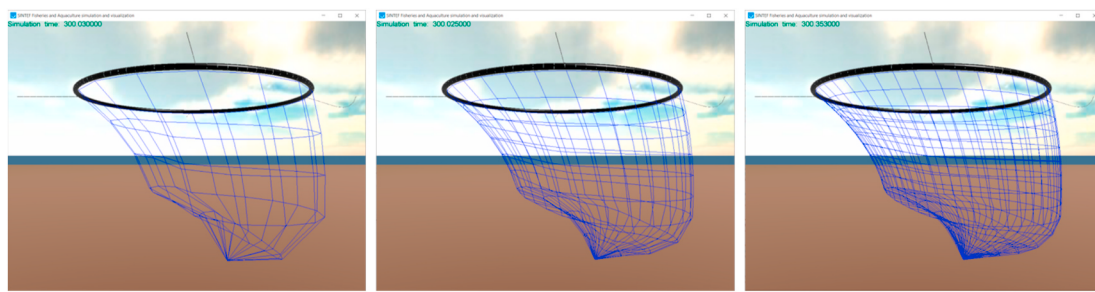


Fig. 11. Simulated steady-state ($U_\infty = 0.5$ m/s, no wave) shapes of the cage with different mesh resolutions. From left to right: $N_H \times N_V = 16 \times 5$ (M1), $N_H \times N_V = 32 \times 10$ (M2), $N_H \times N_V = 48 \times 15$ (M3).

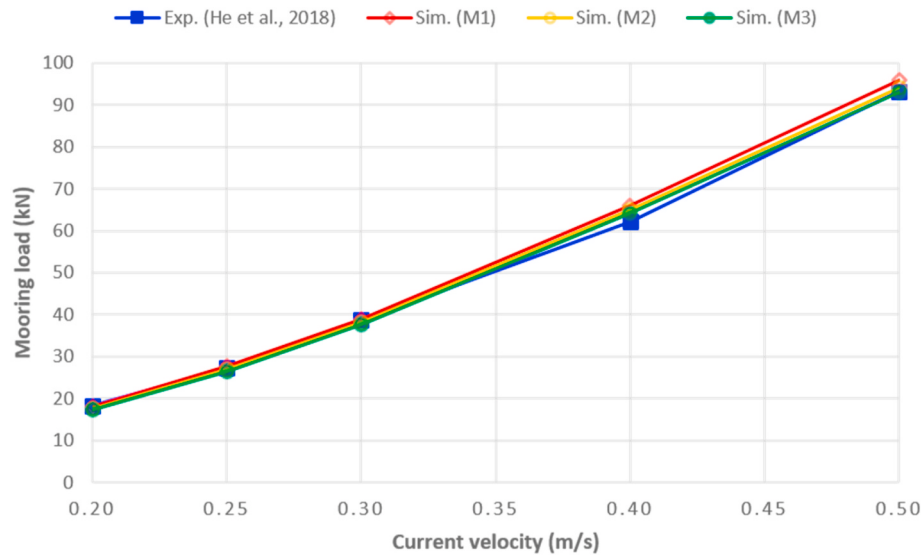


Fig. 12. Simulated mooring loads with different mesh resolutions (M1-3, as shown in Fig. 11) and comparison with the up-scaled experimental data (He et al., 2018).

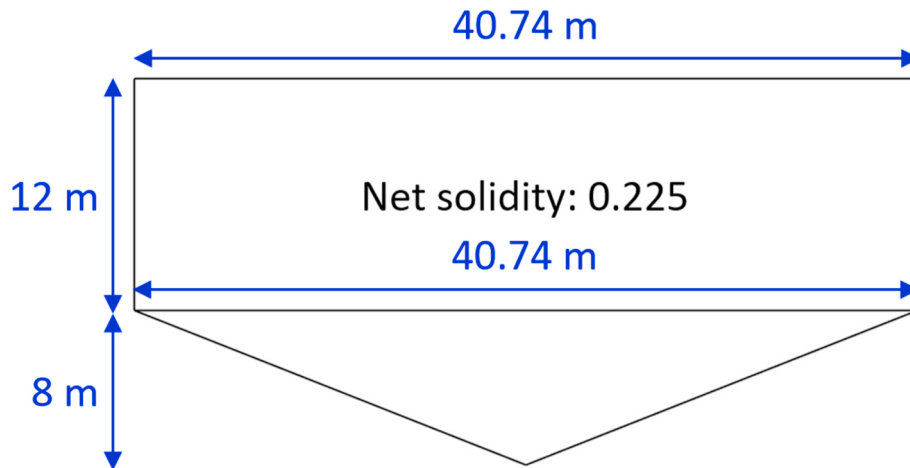


Fig. 13. Sketch of the net cage used in the full-scale measurements (Klebert et al., 2015).

algorithms that optimize bandwidth while ensuring stable communication in the presence of biomass and under various cage environments. A remote-controlled topside computer (through the integrated 4G modem) is used for signal processing and the real-time positioning data can be accessed through a designated URL (Uniform Resource Locator) address.

2.3. Integrated approach for cage monitoring

The use of the extended Kalman filter (Kalman, 1960; Einicke and White, 1999) is firmly entrenched in nonlinear signal processing and state estimation. Based on the extended Kalman filter, a numerical model can be combined with sensor data for a more realistic estimation of the actual system, where the current state estimate is advanced forward in time through the numerical simulation, and is continuously

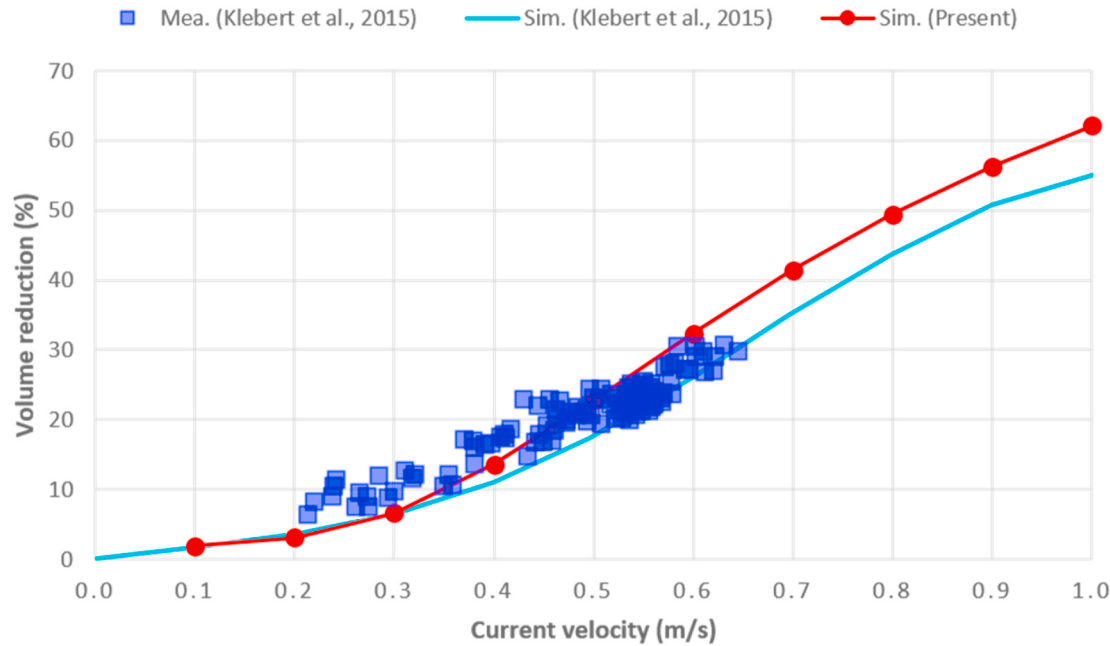


Fig. 14. Simulated cage volume reductions and comparison with the full-scale measurements (Klebert et al., 2015).

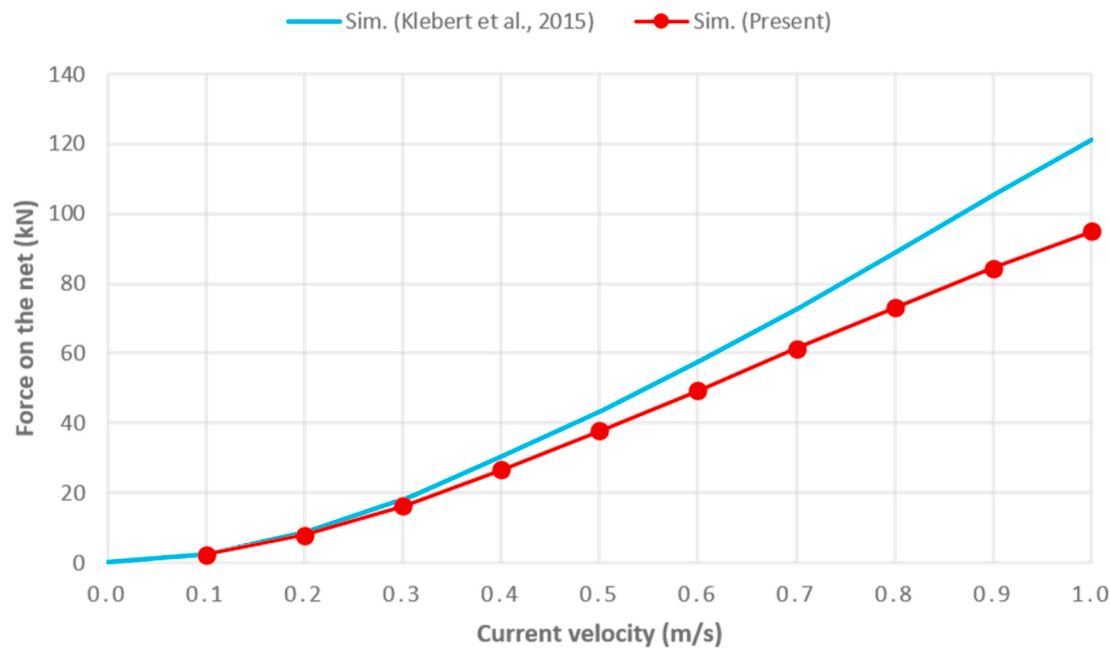


Fig. 15. Simulation results of the forces on the net.

updated to the best possible fit to the sensor data. The numerical simulation model of a net cage typically consists of several hundreds of interconnected nodes (see in Fig. 2), each node has 3 degrees of freedom (DOFs), which means the number of system states is in the order of 10^3 . The numerical implementation of an extended Kalman filter would need to evaluate the state vector covariance matrix, which includes the system Jacobian. Calculation of the system Jacobian of a nonlinear system either needs an explicit expression as a function of the state vector, or a numerical approximation using state perturbations. Both these approaches were found to cause too high computational requirements in a real-time scenario.

In the present study, the measured positions of the net are used to estimate the current velocity profile, i.e. vertical profile of horizontal

flow velocity that is causing the net deformations instead of evaluating and correlating the states of each net node. The blue spheres in Fig. 6 denote measured positions and the white spheres denote simulated positions under an estimated flow condition. Deviations between simulated and measured positions (i.e. position errors) are used to continuously adapt the current velocity profile using a proportional-integral-derivative (PID) controller with integral saturation for each error signal. At each simulation time step, the implemented PID controller calculates the error value, $e(t) \in \mathbb{R}^3$, as the difference between simulated and measured positions, and applies a correction to the magnitude and direction of the incoming current velocity based on the proportional, integral and derivative terms. As illustrated in Fig. 6, the position error $e_i(t)$ is used to estimate the incoming current velocity $U_i(t)$

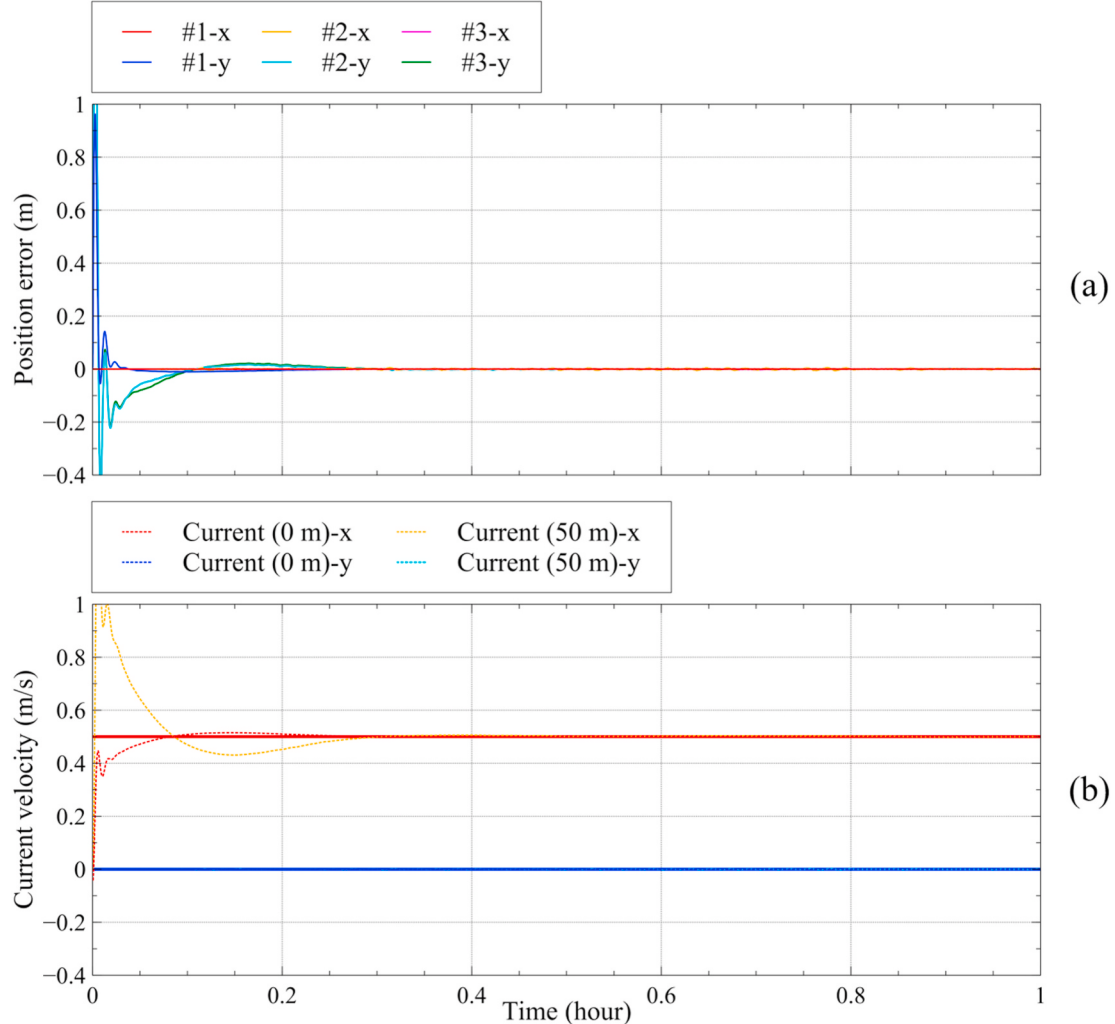


Fig. 16. Estimation results for the “real-world” setup with a uniform current velocity profile (current velocity: 0.5 m/s along the x-axis): (a) Time series showing the differences between the estimated and “real-world” positions; (b) Time series showing the comparisons between the estimated (dotted line) and “real-world” (solid line) current velocities.

at a certain depth d_i , $i = 1, 2, \dots, n$

$$\dot{\mathbf{U}}_i(t) = K_p \mathbf{e}_i(t) + K_i \int_0^t \mathbf{e}_i(\dot{t}) dt + K_d \frac{d\mathbf{e}_i(t)}{dt} \quad (21)$$

where K_p , K_i , and K_d denote the coefficients for the proportional, integral, and derivative terms, respectively. The PID controller is set with integral saturation for preventing the integral term from accumulating above or below pre-defined bounds and an upper limit for the estimated magnitude of current velocity. The incoming current velocity $\mathbf{U}(t)$ at an arbitrary depth d is then calculated as

$$\mathbf{U}(t) = \begin{cases} \mathbf{U}_1(t), & 0 \leq d \leq d_1 \\ \mathbf{U}_1(t) + (\mathbf{U}_2(t) - \mathbf{U}_1(t)) \frac{d - d_1}{d_2 - d_1}, & d_1 < d \leq d_2 \\ \dots, \dots \\ \mathbf{U}_{n-1}(t) + (\mathbf{U}_n(t) - \mathbf{U}_{n-1}(t)) \frac{d - d_{n-1}}{d_n - d_{n-1}}, & d_{n-1} < d \leq d_n \\ \mathbf{U}_n(t), & d_n < d \leq d_{max} \end{cases} \quad (22)$$

which is a piecewise linear approximation of the current velocity profile. Herein, the depth d_i does not need to be same as the depth of each locator. For instance, a locator deployed at 5 m depth can be used to

estimate the incoming current velocity at 0 m depth. The piecewise linear approximation does not need to satisfy the flow condition at the bottom boundary layer d_{max} , since it has no effect on the simulated net deformation if the last depth layer d_n is set to be larger than the total depth of the cage. However, if the measured net position (e.g. Position error $\mathbf{e}_3(t)$ as shown in Fig. 6) is affected by the alteration of the flow beneath the cage (e.g. due to the interaction with the bottom of the sea as reported by Klebert et al. (2015)), the estimation result of the current velocity beneath the cage (i.e. $\mathbf{U}_n(t)$) will also be affected. Furthermore, the alteration of the flow due to the interaction with the cage can, to a certain extent, be reflected in the estimated current velocities as they are determined by the measured actual net positions.

As mentioned in Section 2.2, the measurements made by the SBL system are relative to the positions of the baseline transducers mounted on the floating collar. In practice, this means that the measurements provided by the locators placed at three different depths will be relative to the surface, implying that eventual dynamics exhibited by the floating collar or mooring components will have little impact on the position measurements. This further suggests that the numerical model does not need to represent these components. A simplification of the cage model (as shown in Fig. 6) enables its use in real-time simulations where online measurement data are incorporated through the implemented TCP/IP (Transmission Control Protocol/Internet Protocol) interface. At each moment (e.g. every 0.1 s), a piecewise linear current velocity profile is

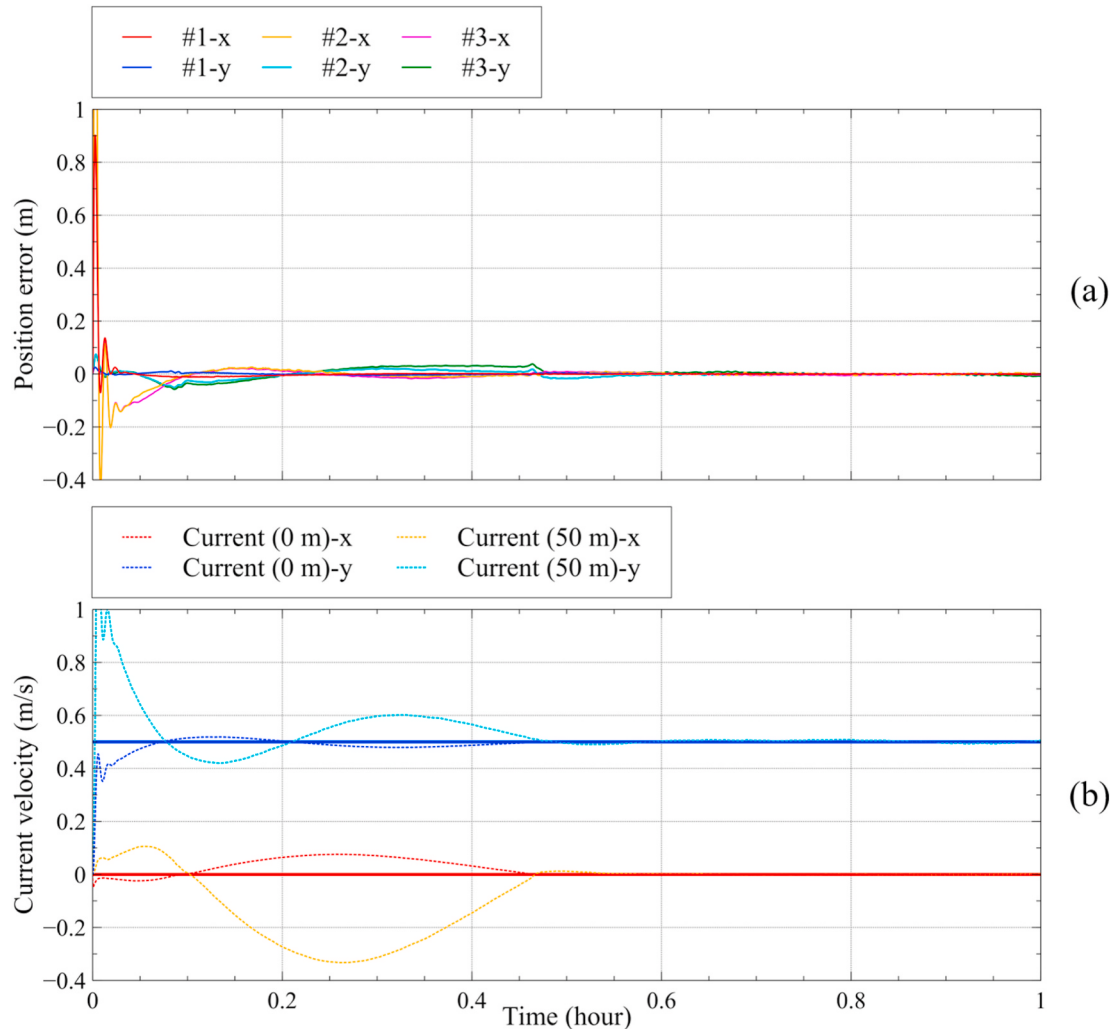


Fig. 17. Estimation results for the “real-world” setup with a uniform current velocity profile (current velocity: 0.5 m/s along the y-axis): (a) Time series showing the differences between the estimated and “real-world” positions; (b) Time series showing the comparisons between the estimated (dotted line) and “real-world” (solid line) current velocities.

estimated and simultaneously applied in the simulation of net cage deformations, resulting in a gradual convergence towards the best possible fit to the measurement data.

3. Convergence studies and model validations

Two numerical case studies were conducted to evaluate the convergence and accuracy of the numerical simulation model. The simulated hydrodynamic forces and cage deformations were compared with existing model-scale experimental data (He et al., 2018) and full-scale measurements (Klebert et al., 2015). Simulated positioning data were also used to verify the proposed integrated approach for cage monitoring, by comparing estimated current velocity profiles with those provided in the simulations.

3.1. Hydrodynamic forces and resultant mooring loads

Fig. 7 shows the main dimensions of the net cage used by He et al. (2018) in the model-scale (1:25) experiments which were conducted according to Froude scaling. Corresponding full-scale dimensions were used in the numerical simulations, as the main objective of using these data was to check the convergence of the numerical simulation model with respect to full-scale mesh resolutions and integrator time steps. It should also be mentioned that the net twine diameter was 0.6–0.8 mm in

the model-scale experiments, which implies that the Reynolds number with twine diameter as characteristic length was not properly scaled. This effect was considered to be secondary if the correct solidity ratio was used (He et al., 2018). In the present paper, the experimental data are scaled up for the comparison with the numerical simulation results, while the scaling effect is not further discussed.

The time steps used in the simulations based on He et al. (2018) ranged from 0.001 to 0.1 s and a combined current and wave condition was applied: current velocity $U_\infty = 0.5$ m/s; significant wave height $H_s = 2$ m; mean wave period $T_p = 6$ s. For testing the convergence of the net model alone, the net was assumed to be fixed on top (see in Fig. 8) without including other structural components, such as a floating collar. Fig. 9 shows the simulated time series of the total drag forces on the net, where different time steps were used ($\Delta t = 0.001 \sim 0.1$ s). The corresponding mean and significant (i.e. the mean of the highest one-third peaks) values of the drag forces are shown in Fig. 10. By comparing these results, it is evident that the net model has good convergence abilities, especially when looking at the mean values, with a maximum of 4% deviation for all tested time steps. The convergence of the significant values is also considered to be good. When a time step of 0.001 s was used, the implemented kinematic constraints (as described in Section 2.12) were close to the elastic stiffness of the truss elements. Thus, the elastic modes of the truss elements were maintained, resulting in accurate estimations of structural response and hydrodynamic forces.

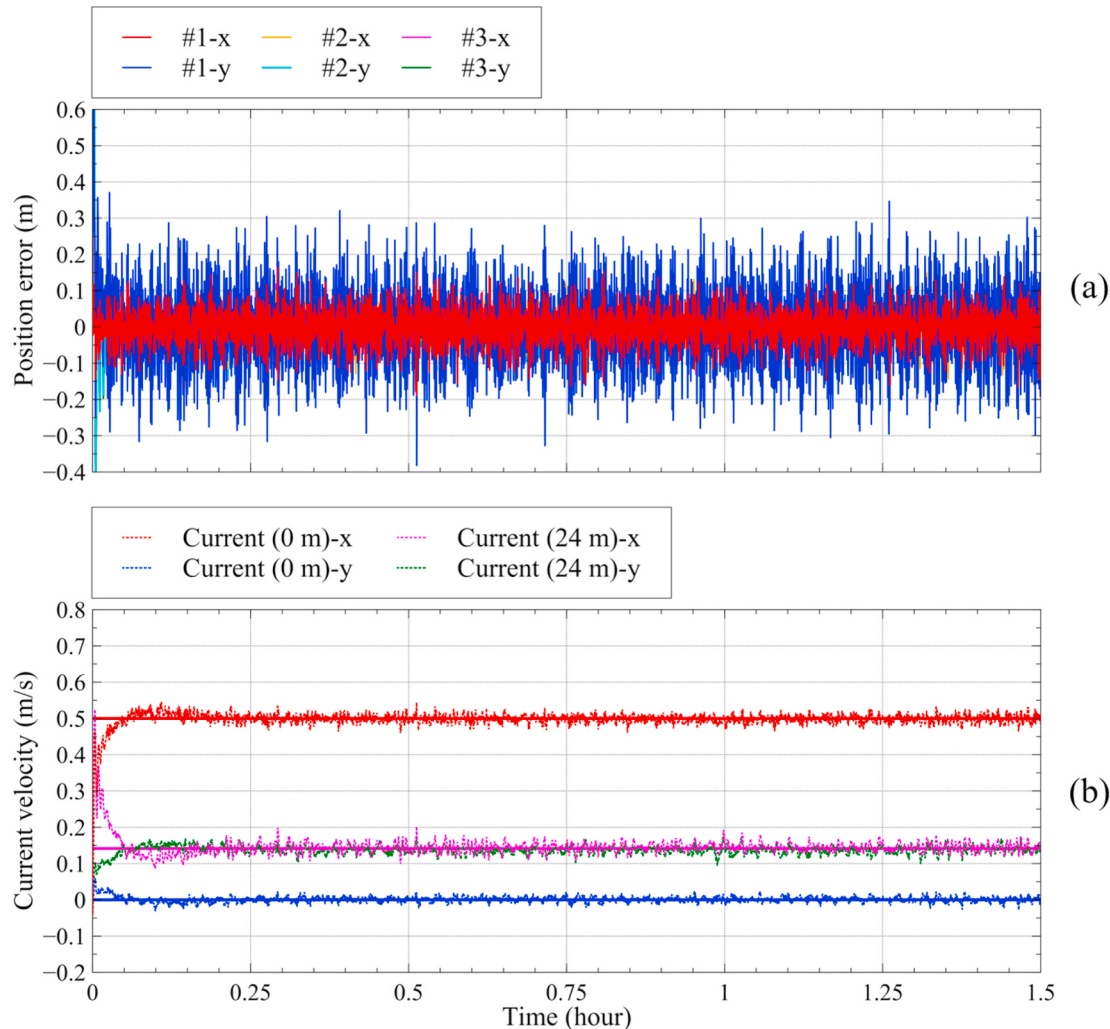


Fig. 18. Estimation results for the “real-world” setup with a one-layer linear current velocity profile (current velocity at 0 m depth: 0.5 m/s along the x-axis; current velocity at 24 m depth: 0.2 m/s oriented at 45° to the x-axis) and an irregular wave field ($H_s = 1$ m; $T_p = 5$ s): (a) Time series showing the differences between the estimated and “real-world” positions; (b) Time series showing the comparisons between the estimated (dotted line) and “real-world” (solid line) current velocities.

When a time step of 0.1 s was used, the high-frequency axial dynamics of the truss elements were filtered out due to the stability requirement. This caused about 16% overestimation of the significant forces, but also resulted in a positive effect that the simulation was more than 10 times faster than real-time. When a time step of 0.01 s was used, the simulation was still about 1.5 times faster than real-time, while giving good estimates of both the mean (3% deviation) and significant (7% deviation) forces.

Fig. 11 shows three different mesh resolutions of the net cage that were used in the convergence study with respect to the mooring loads, where $N_H \times N_V$ denote the number of truss elements in the horizontal and vertical directions, respectively. A floating collar and a simple mooring system were also included in these simulations, according to the experimental setup (He et al., 2018). In Fig. 12, the simulation results (i.e. mooring loads versus current velocities) are shown to be insensitive to the mesh configuration and agree well with the up-scaled experimental data using Froude scaling. As previously validated (Kristiansen and Faltinsen, 2012, 2015; Shen, 2018), the screen force model with the velocity reduction factor suggested by Løland (1991) can together provide a very good estimation of the steady-flow (i.e. current) forces acting on the net.

3.2. Cage deformations

Fig. 13 shows the main dimensions of the net cage used by Klebert et al. (2015) in full-scale experiments, where cage deformations were measured using 19 pressure tags attached around the net at different depths, and 6 around the sinker tube. Cage volume reductions under different flow conditions were calculated based on the measurement data and simulations using a sophisticated model of the net (Endresen et al., 2014). In the present simulations, the simplified net cage model described above was used, and the calculated volume reductions were compared with the full-scale measurements and the simulation results given in Klebert et al. (2015). As shown in Fig. 14, the overall comparison is good, but the present simulations seem to underestimate the volume reductions for low current velocities (0.2–0.3 m/s). As mentioned in Klebert et al. (2015), some fouling on the net was observed in the full-scale experiments, which was corresponding to the low current velocities and could lead to larger deformations due to the increased forces. During the full-scale experiments, the force on the cage was not measured, but the result from the simulation was reported. Fig. 15 compares the present simulation with the result shown in Klebert et al. (2015) where a Morison type of force model was used for the net. Herein, the Morison model is found to predict higher forces than the present model, especially for highly deformed nets, while the present simulation shows larger volume reduction than the Morison model. The

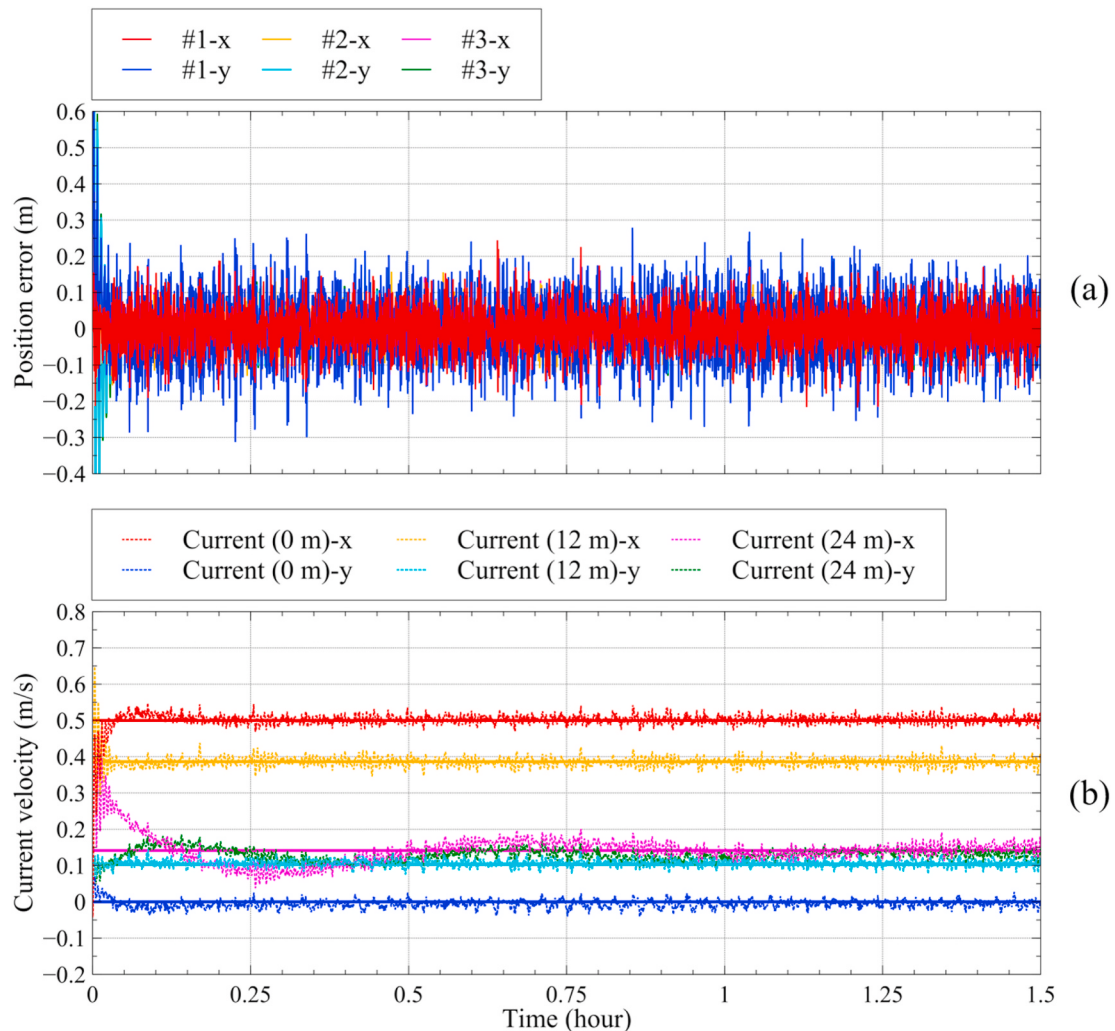


Fig. 19. Estimation results for the “real-world” setup with a two-layer linear current velocity profile (current velocity at 0 m depth: 0.5 m/s along the x-axis; current velocity at 12 m depth: 0.4 m/s oriented at 15° to the x-axis; current velocity at 24 m depth: 0.2 m/s oriented at 45° to the x-axis) and an irregular wave field ($H_s = 1$ m; $T_p = 5$ s): (a) Time series showing the differences between the estimated and “real-world” positions; (b) Time series showing the comparisons between the estimated (dotted line) and “real-world” (solid line) current velocities.



Fig. 20. Deployment of the SBL based positioning system at a full-scale fish farm site (corresponding to Fig. 1), with three locators mounted on a cage at different depths, measuring the horizontal positions of the net.

same findings have been reported by Kristiansen and Faltinsen (2012) when the screen force model was introduced for the calculation of the force on the net and the estimation of volume reduction. In the present paper, the improved accuracy for the simulation of net cage deformation via the screen force model and the comparison with the Morison type of force model are not further discussed.

3.3. Instantaneous current velocity profiles

Before considering the field deployments, the integrated approach

for cage monitoring (as described in Section 2.3) was tested using a pair of experiments simulating the full-scale net cage structure in Klebert et al. (2015). The first simulation was set up with a known current velocity profile, resulting in cage deformations that were considered the “real-world” simulation. The second simulation was then set up without a pre-defined current velocity profile and rather set up to use the positions of three selected nodes from the former simulation as inputs to the integrated current estimation structure. The selected nodes (#1, #2, and #3) were located at 4 m, 12 m, and 20 m depths, and they were distributed along the x-axis, i.e. $x_1 = 20.37$ m, $x_2 = -20.37$ m, and

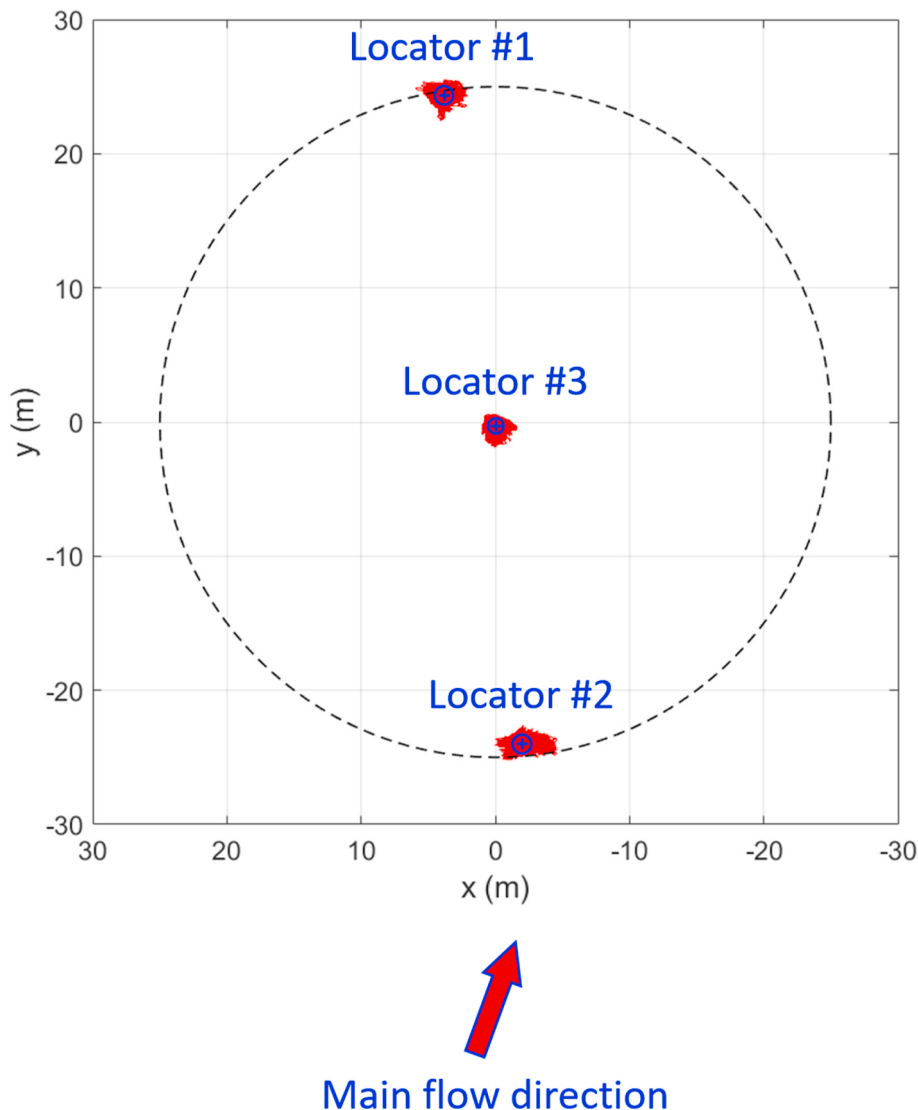


Fig. 21. Trajectories (marked by red lines) of the locators and the calculated mean positions (marked by blue crosses) and standard deviations (marked by blue circles) during a selected tidal period. (For interpretation of the references to colour in this figure legend, the reader is referred to the Web version of this article.)

$x_3 = 0$ m, while $y_{1,2,3} = 0$ m. As shown in Fig. 6, the x and y components of the calculated position errors (i.e. $e_1(t)$, $e_2(t)$, and $e_3(t)$) were used to estimate the x and y components of current velocities at different depths. This enabled real-time estimation of the vertical profile of horizontal flow velocity and comparison with the “real-world” setup.

When the “real-world” simulation was set up with a uniform current velocity profile (i.e. 0.5 m/s throughout the depth), the magnitude and direction (i.e. along the x-axis) of the current were correctly estimated based on the input “real-world” positions from one of the selected nodes, and the accuracy of the estimation result was unaffected by the location of the node (i.e. #1, #2, or #3). As shown in Fig. 16, the position error of node #1 (located at 4 m depth) was used to estimate the current velocity at 0 m depth, and the position error of node #2 (located at 12 m depth) was used to estimate the current velocity at 50 m depth. The estimation results at 0 m and 50 m depths were found to be the same and coincide with the “real-world” setup when the position errors converged to zero. As shown in Fig. 17, the estimation results also converged to the “real-world” values when the current direction was altered by 90° (i.e. along the y-axis), but more computational efforts were required (i.e. the estimation results took more time to converge). This indicates that the efficiency of the estimation model will depend on the configuration of the positioning sensors. If there is a main flow direction at the fish farm site,

it will be more efficient to deploy the positioning sensors along this direction (see e.g. in Fig. 6).

When the “real-world” simulation was set up with a one-layer linear current velocity profile (current velocity at 0 m depth: 0.5 m/s along the x-axis; current velocity at 24 m depth: 0.2 m/s oriented at 45° to the x-axis), the current velocities at the two different depths were correctly estimated, even with disturbances from the waves (irregular waves: $H_s = 1$ m; $T_p = 5$ s). As shown in Fig. 18, the position error of node #1 (located at 4 m depth) was used to estimate the current velocity at 0 m depth, and the position error of node #3 (located at 20 m depth) was used to estimate the current velocity at 24 m depth. The mean values of the estimated positions and current velocities were found to coincide with the “real-world” setup, and the transient position errors were below 0.4 m, which was attributed to the disturbances from the waves.

Fig. 19 shows the estimation results for the “real-world” setup with a two-layer linear current velocity profile, where the first depth layer (0–12 m) was set in accordance with the cylindrical part of the cage and the second depth layer (12–24 m) was set to cover the conical bottom of the cage. The position errors of the three selected nodes, #1, #2, and #3, were used to estimate the current velocities at 0 m, 12 m, and 24 m depths, respectively. This was found to be an optimal setup for the integrated estimation structure considering both the accuracy and the

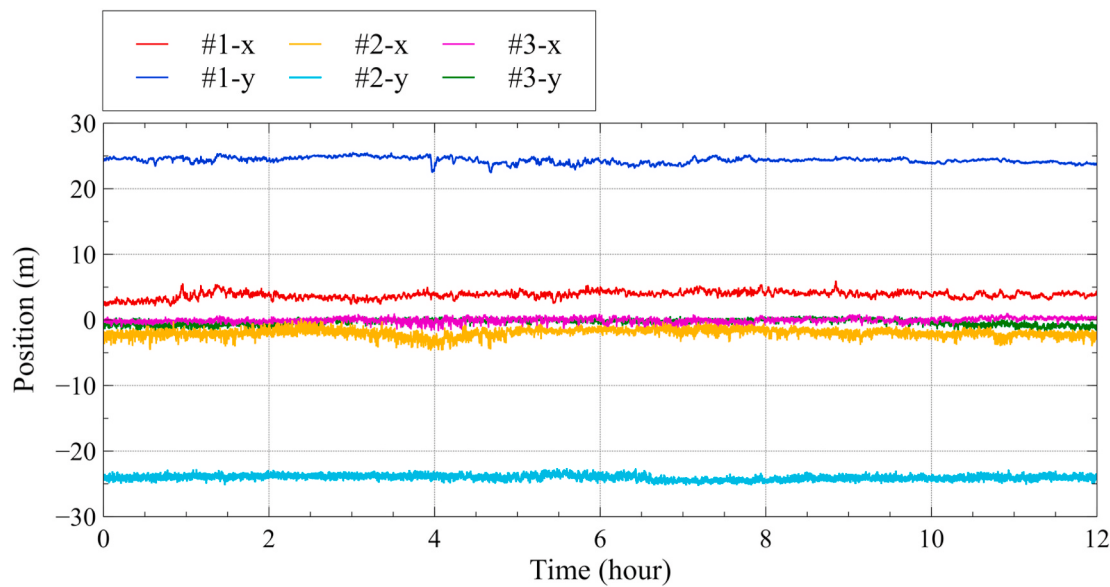


Fig. 22. Time series of the measured positions during a selected tidal period (corresponding to Fig. 21).

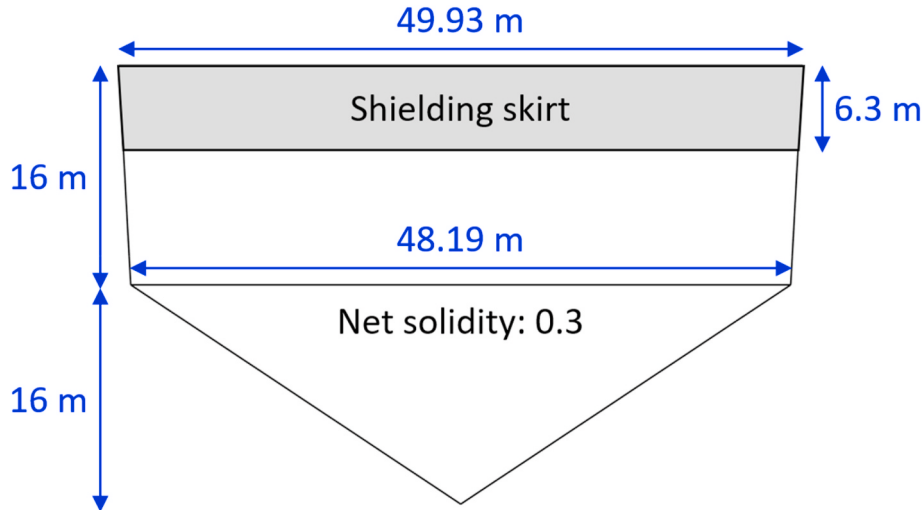


Fig. 23. Sketch of the net cage used in the numerical simulation model for cage monitoring.

computational effort. A more representative current velocity profile could be predicted by use of more positioning sensors. However, as shown in Figs. 18 and 19, it could also result in a significant increase in convergence time, due to the increased number of interdependent states in the estimation model.

4. Field deployments and monitoring results

The SBL based positioning system was deployed at a full-scale fish farm site (Fig. 20), with three locators mounted on a cage at 6.3 m (lower edge of the shielding skirt), 16 m (connection to the sinker tube), and 32 m (connection to the bottom weight) depths, measuring the horizontal positions of the net. Fig. 21 shows the trajectories of the locators and the calculated mean positions and standard deviations during a selected tidal period (i.e. 12 h). The diameter of this cage was approximately 50 m, which is marked by the dashed-line circle. Corresponding time series (1 Hz logging rate) for the measured locator positions (Fig. 22) do not show large variations, except for possible disturbances from water waves and measurement noise not handled by the signal processing algorithms. The calculated mean positions of

Locator #1 and Locator #2 during this period were used to determine the actual cage diameter at the two different depths for the setup of the numerical simulation model. The main dimensions of the net cage that were used in the simulation model and the corresponding configuration of the locators are shown in Fig. 23 and Fig. 24, respectively. The half mesh width of the net was 17.5 mm with a twine diameter of 2.5 mm. Effective net solidity was set to 0.3 to account for possible fouling on the net. Since only steady-flow forces and the resultant net deformations were of interest, a simulation time step of 0.1 s and moderate mesh resolution ($N_H \times N_V = 48 \times 12$) were used. There was also a shielding skirt (for preventing sea lice) installed at 0–6.3 m depth in the cage. As the screen force model is only applicable for $S_n \leq 0.5$, the hydrodynamic forces acting on the shielding skirt were calculated by assuming $c_d = 1$ in Eq. (16) to Eq. (19).

Fig. 25 shows the time series of the measured positions during the selected three tidal periods when the locators had largest displacements, smoothed using 10-min moving average to limit the effects of transient disturbances and measurement noise. The 10-min steady-state data were incorporated into the numerical simulation model for the estimation of current velocities and cage deformations. Fig. 26 shows the estimation

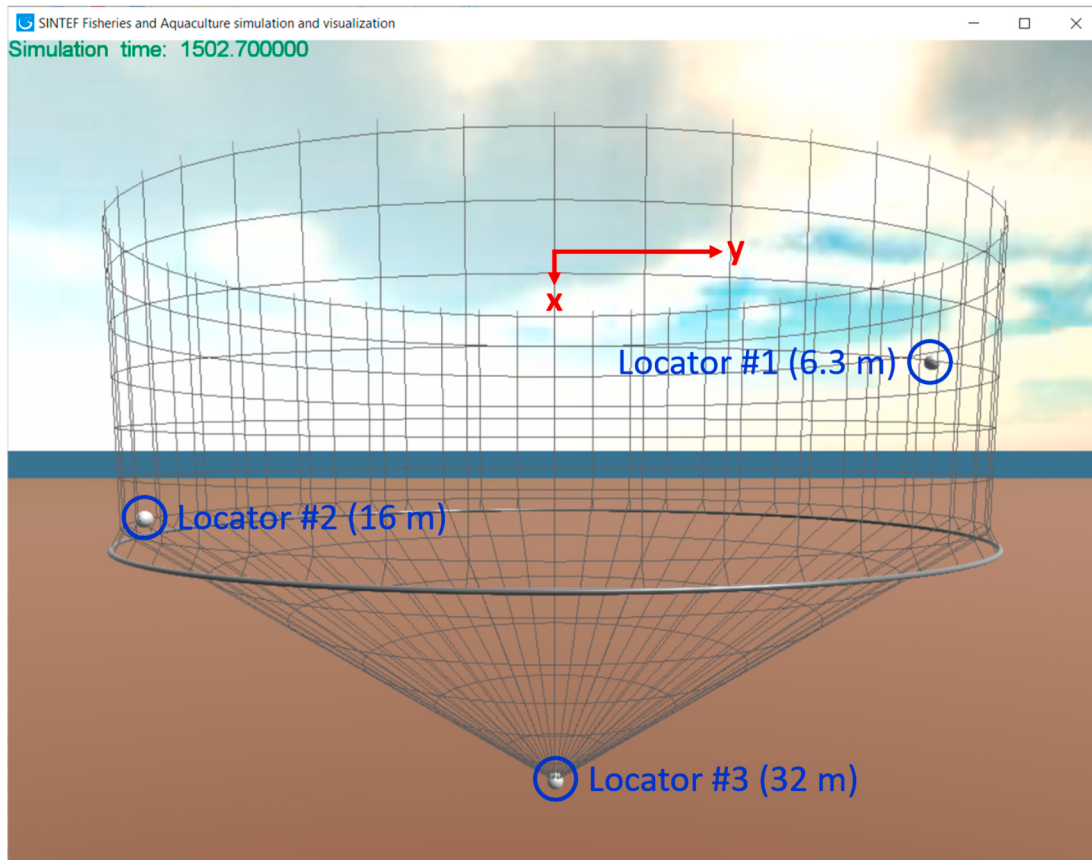


Fig. 24. Configuration of the locators in the numerical simulation model.

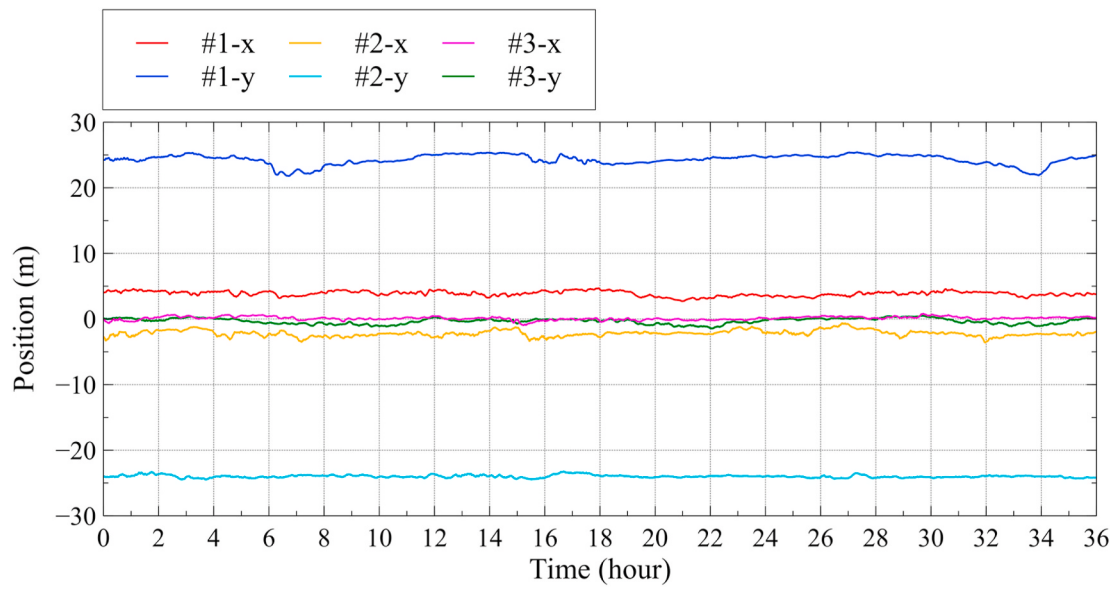


Fig. 25. Time series of the measured positions (10-min moving average) during the selected three tidal periods.

results when two locators (Locator #1 and Locator #3) were used, and Fig. 27 shows the estimation results when all the three locators were used. While the maximum position error was about 1.7 m when two locators were used, it was lower at about 0.6 m when using three locators. This was because using three locators improved the current velocity profile estimation from a one-layer profile (Fig. 26b) to two-layer profile (Fig. 27b). Cage volume estimations were also quite different

with three locators (Fig. 27c) than when using two (Fig. 26c). Maximum volume reduction was about 12% when the cage encountered a 0.4 m/s tidal flow between the 6th and 8th hour (Fig. 27c). The shape of the cage during this period indicated a significant variation of current directions and magnitudes along the two depth layers (0–16 m and 16–32 m, Fig. 28). This variation could be attributed to the complex interactions between the current flow and the cage (Lader et al., 2008) and other

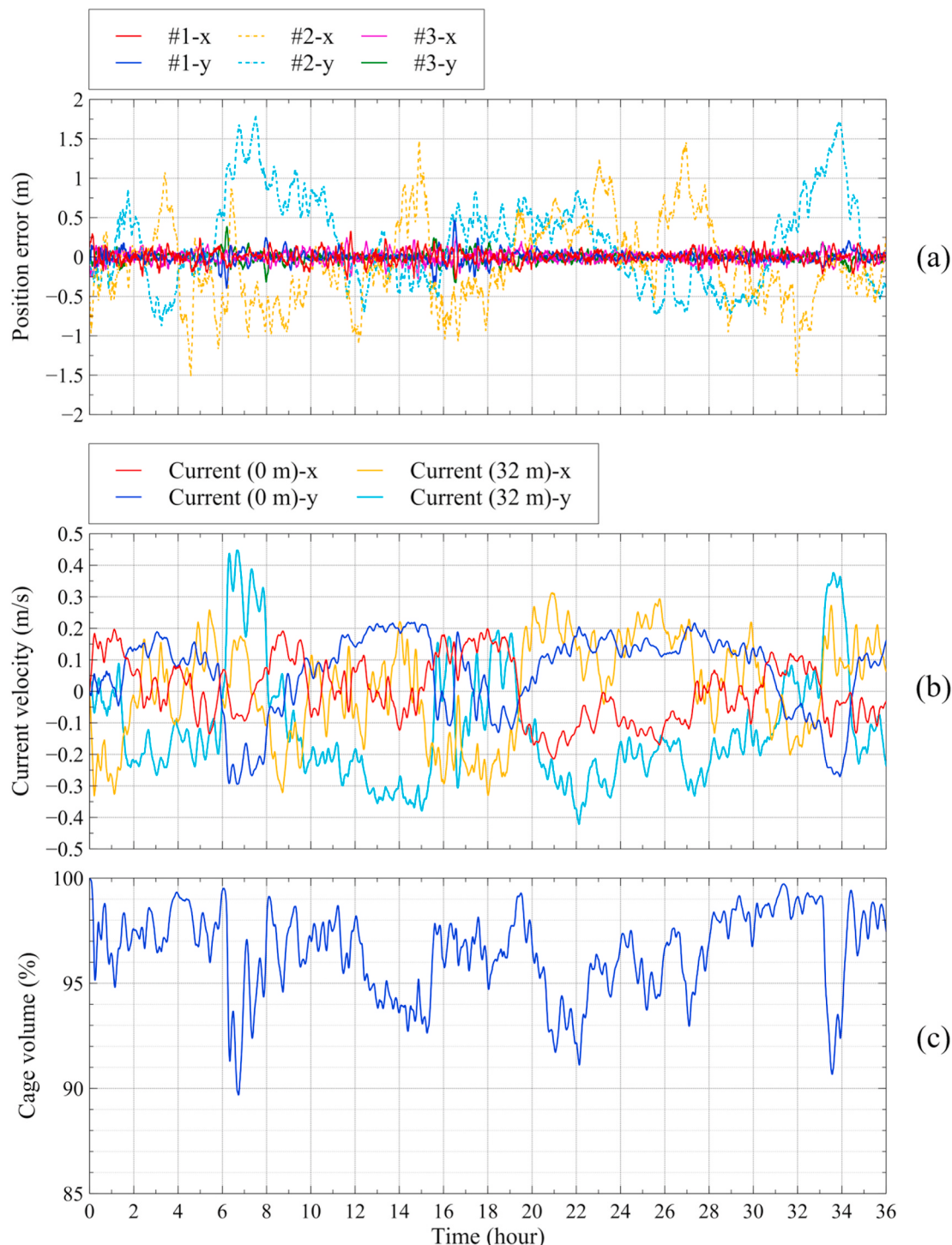


Fig. 26. Estimation results when two locators were used. (a) Time series showing the differences between the estimated and measured positions. (b) Time series of the estimated current velocity profiles. (c) Time series of the estimated cage volumes.

influences such as local topography and the layout of the fish farm site (Klebert et al., 2015). As shown in Fig. 20, when the current was coming from the right-hand side (i.e. along the positive y-axis) there was a shielding effect due to the cages on the upstream side (Fig. 20), while there was no shielding when the current was coming from the left-hand side (i.e. along the negative y-axis). This can explain why the magnitudes of the estimated current velocities were about 25% lower when they were positive (Fig. 27b). The estimated current velocities at 0 m depth also correlated with the three tidal periods and were comparable to the measured flow conditions at this fish farm site (Klebert and Su,

2020). However, there was no directly available data for the validation of present estimation results.

When the positioning data were further smoothed using a 1-h moving average, the instantaneous estimation errors were below 0.3 m during the three tidal periods (Fig. 29 and Fig. 30). Compared with the maximum estimation errors when using raw data at 1 Hz (about 3 m) and when using a 10-min moving average (about 0.6 m), this demonstrates how transient disturbances (e.g. waves and fish farm operations) and measurement noise can affect the monitoring and estimation results. Since the present positioning system could not capture these transient

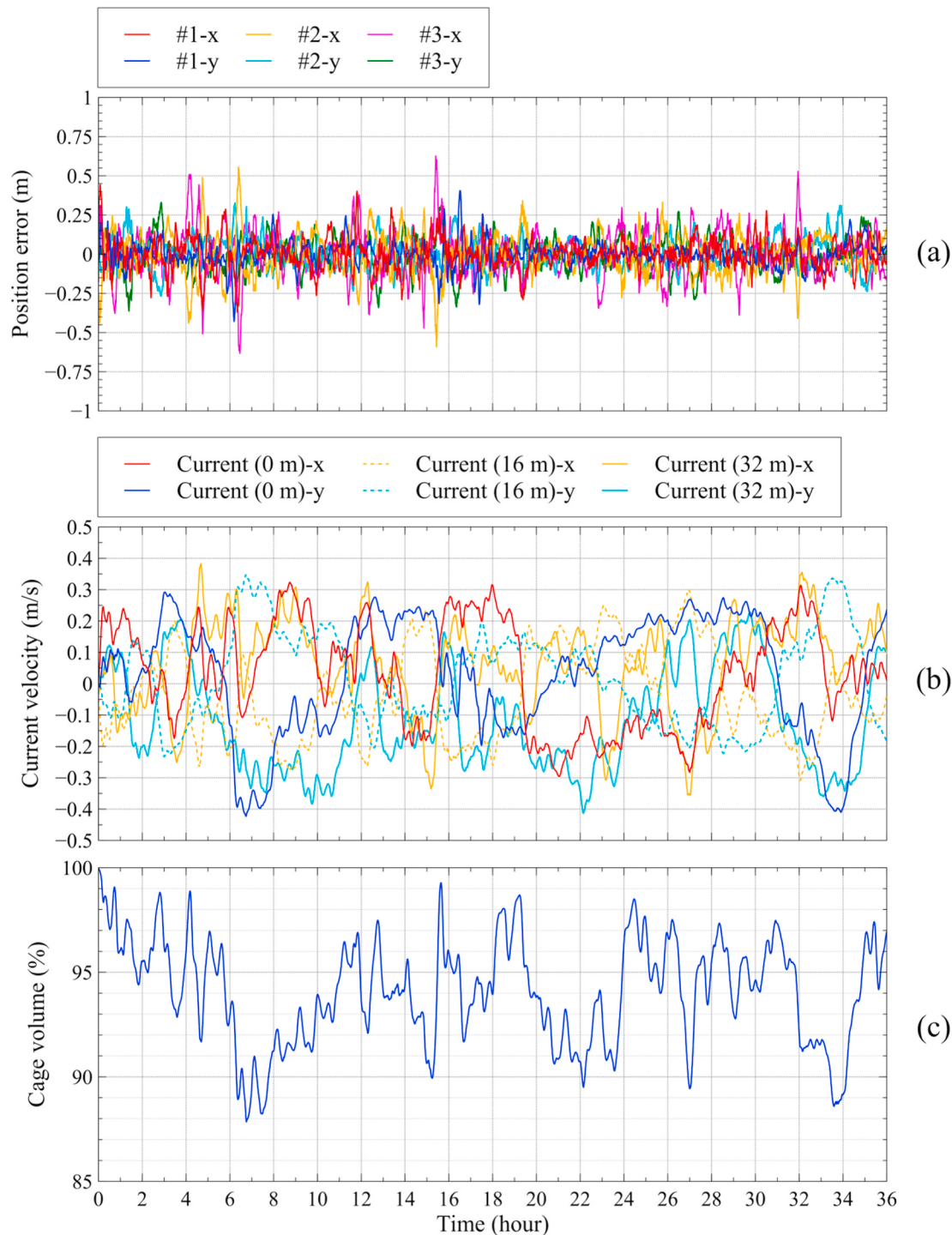


Fig. 27. Estimation results when three locators were used. (a) Time series showing the differences between the estimated and measured positions. (b) Time series of the estimated current velocity profiles. (c) Time series of the estimated cage volumes.

states, only the steady-state data could be used in the integrated estimation model. Furthermore, the requirements for real-time communication and long-term data acquisition restrict the number of acoustic sensors that can be used at a full-scale fish farm site. The setup of three locators in accordance with the cylindrical-conical shape (as shown in Fig. 24) of the cage is shown to be able to predict a two-layer linear current velocity profile and the resulting cage deformation. This is considered to be sufficient for general-purpose monitoring and well suited for real-time applications.

5. Conclusions

In the present study, an integrated approach that combines a numerical model and positioning sensor data was developed for real-time monitoring of net cage deformations. An SBL based positioning system was deployed at a full-scale fish farm site and the integrated estimation model was tested with the obtained in-situ measurement data. The main objective of the numerical and experimental study was to demonstrate the potential use of an optimal setup of the integrated system for in-situ real-time monitoring. The main achievements and findings of the study

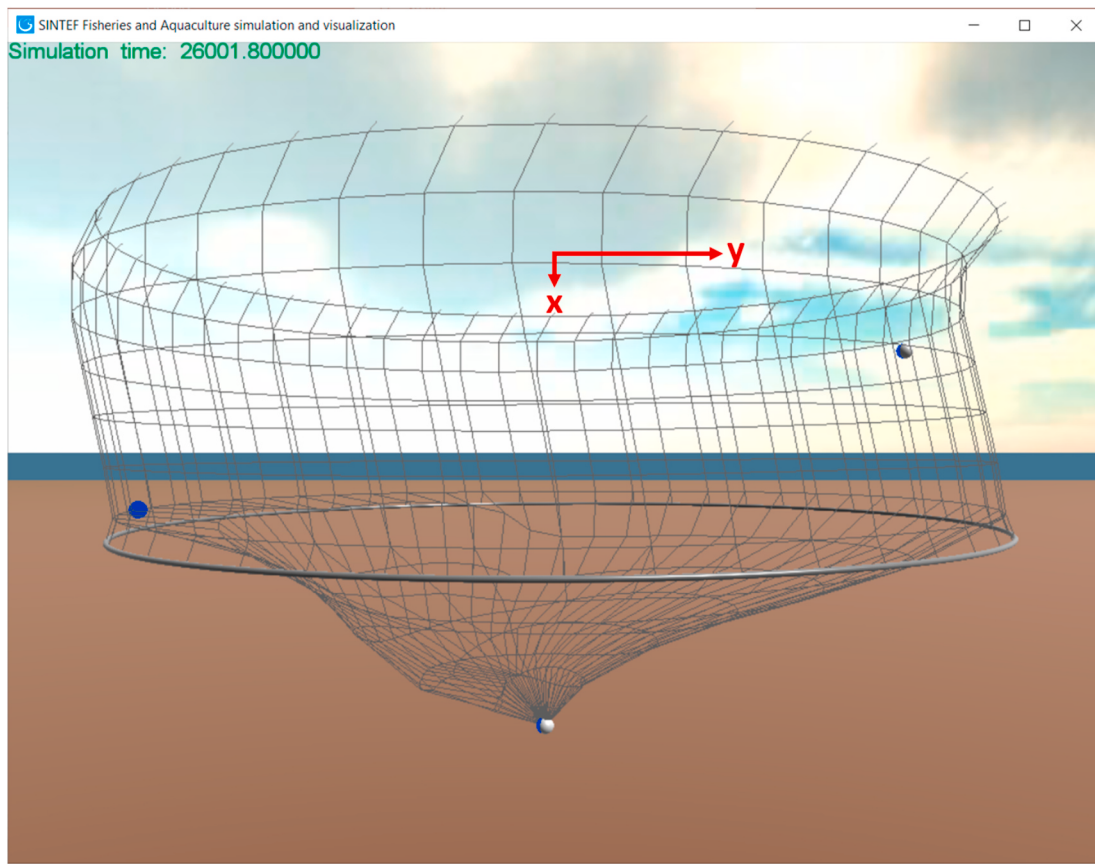


Fig. 28. Estimated instantaneous (between the 6th and 8th hour) shape of the cage when three locators were used.

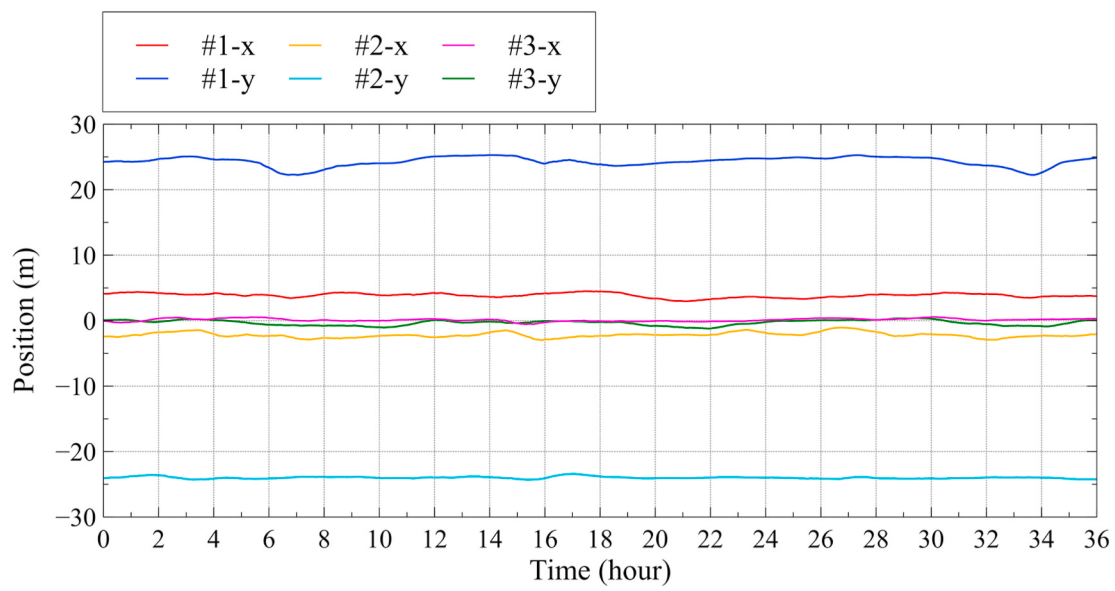


Fig. 29. Time series of the measured positions (1-h moving average) during the selected three tidal periods.

are as follows:

- A real-time numerical simulation model of aquaculture net cage was established based on the Baumgarte stabilization method for constrained multibody dynamics.

- The implemented screen force model was considered to, in part, account for fluid–structure interaction and integrated flow effects on the net by using experimentally based force coefficients.
- The accuracy and convergence performance of the numerical simulation model were verified through comparisons with existing model-scale and full-scale experimental data.

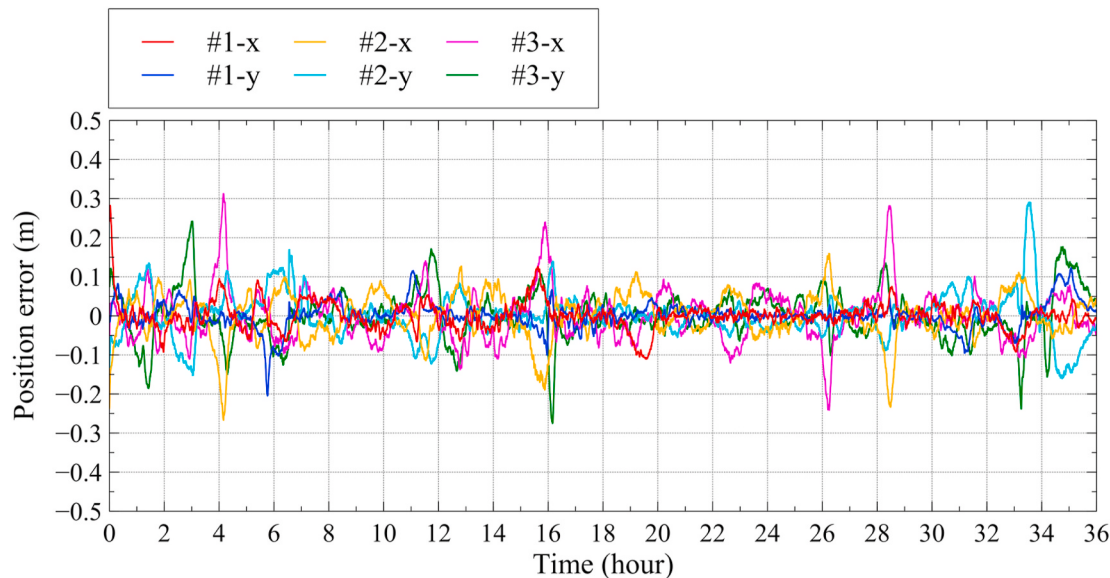


Fig. 30. Time series showing the differences between the estimated and measured positions (1-h moving average) when three locators were used.

- The accuracy and efficiency of the integrated estimation model were evaluated through a set of simulated experiments, and they were found to be dependent on the number and configuration of the positioning sensors.
- The in-situ monitoring results were affected by transient disturbances and measurement noise, only the steady-state sensor data could be used in the integrated estimation model.
- The setup of three acoustic sensors in accordance with the cylindrical-conical shape of the cage was shown to be able to predict a two-layer linear current velocity profile, resulting in a best possible estimation of cage deformation in real-time.
- More testing and validation data are needed for quantitative evaluation of cage deformation and the accuracy of in-situ monitoring results.

In conclusion, the proposed approach is found to be well suited for general-purpose monitoring of net cage deformations. It can be further developed, in case higher accuracy is required, by using a combination of different sensors (e.g. inertial measurement unit (IMU), acoustic and depth sensors) and a 3D interpolation algorithm for reconstructing complex flow conditions around and beneath the cage.

CRediT authorship contribution statement

Biao Su: Conceptualization, Methodology, Software, Validation, Investigation, Writing - original draft. **Eleni Kelasidi:** Formal analysis, Investigation, Writing - review & editing. **Kevin Frank:** Conceptualization, Investigation, Resources, Writing - review & editing. **Joakim Haugen:** Methodology, Software, Writing - review & editing. **Martin Føré:** Conceptualization, Investigation, Writing - review & editing. **Magnus Oshaug Pedersen:** Investigation, Resources, Visualization.

Declaration of competing interest

The authors declare that they have no known competing financial interests or personal relationships that could have appeared to influence the work reported in this paper.

Acknowledgements

This work was financed by the Research Council of Norway through the project: Development of technology for autonomous, bio-interactive

and high-quality data acquisition from aquaculture net cages (CageReporter, project number 269087). The underwater positioning system used in the field experiments was developed by Water Linked AS. We would like to thank Water Linked AS, Sealab AS, Norsk Havservice AS and Norwegian University of Science and Technology (NTNU) for their contributions in this project.

References

- Aarsnes, J.V., Løland, G., Rudi, H., 1990. Current forces on cage, net deflection. *Engineering for Offshore Aquaculture*. Thomas Telford, Glasgow, pp. 137–152.
- Arnesen, B.O., Sandøy, S.S., Schjølberg, I., Alfredsen, J.A., Utne, I.B., 2018. Probabilistic localization and mapping of flexible underwater structures using Octomap. *Proceedings of the 2018 European Control Conference (ECC)*.
- Berstad, A.J., Heimstad, L.F., Walaunet, J., 2014. Model testing of fish farms for validation of analysis programs. *Proceedings of the ASME 2014 33rd International Conference on Ocean, Offshore and Arctic Engineering*.
- Bi, C.W., Zhao, Y.P., Dong, G.H., Zheng, Y.N., Gui, F.K., 2014. A numerical analysis on the hydrodynamic characteristics of net cages using coupled fluid-structure interaction model. *Aquacult. Eng.* 59, 1–12.
- Cheng, H., Li, L., Aarsæther, K.G., Ong, M.C., 2020. Typical hydrodynamic models for aquaculture nets: a comparative study under pure current conditions. *Aquacult. Eng.* 90 (2020), 102070.
- DeCew, J., Fredriksson, D.W., Lader, P.F., Chambers, M., Howell, W.H., Osienki, M., Celikkol, B., Frank, K., Høy, E., 2013. Field measurements of cage deformation using acoustic sensors. *Aquacult. Eng.* 57 (2013), 114–125.
- Endresen, P.C., Birkevold, J., Føré, M., Fredheim, A., Kristiansen, D., Lader, P.F., 2014. Simulation and validation of a numerical model of a full aquaculture net-cage system. *Proceedings of the ASME 2014 33rd International Conference on Ocean, Offshore and Arctic Engineering*.
- Einicke, G.A., White, L.B., 1999. Robust extended Kalman filtering. *IEEE Trans. Signal Process.* 47 (9), 2596–2599.
- Filgueira, R., Guyonnet, T., Reid, G.K., Grant, J., Cranford, P.J., 2017. Vertical particle fluxes dominate integrated multi-trophic aquaculture (IMTA) sites: implications for shellfish-fishfin synergy. *Aquaculture Environment Interactions* 9 (1), 127–143.
- Fredheim, A., 2005. Current Forces on Net Structures. Doctoral Thesis, Department of Marine Technology, Norwegian University of Science and Technology, Norway.
- Føré, M., Frank, K., Norton, T., Svendsen, E., Alfredsen, J.A., Dempster, T., Eguiraun, H., Watson, W., Stahl, A., Sunde, L.M., Schellewald, C., Skoien, K.R., Alver, M.O., Berckmans, D., 2018. Precision fish farming: a new framework to improve production in aquaculture. *Biosyst. Eng.* 173, 176–193.
- Goldstein, S., 1965. *Modern Developments in Fluid Dynamics*. Dover Publications.
- He, Z., Faltinsen, O.M., Fredheim, A., Kristiansen, T., 2018. The influence of fish on the mooring loads of a floating net cage. *J. Fluid Struct.* 76, 384–395.
- Huang, C.C., Tang, H.J., Liu, J.Y., 2006. Dynamical analysis of net cage structures for marine aquaculture: numerical simulation and model testing. *Aquacult. Eng.* 35 (3), 258–270.
- Huang, C.C., Tang, H.J., Liu, J.Y., 2007. Modelling volume deformation in gravity-type cages with distributed bottom weights or a rigid tube-sinker. *Aquacult. Eng.* 37 (2), 144–157.
- Kalman, R.E., 1960. A new approach to linear filtering and prediction problems. *Transactions of the ASME Journal of Basic Engineering* 82 (Series D), 35–45.

- Kelasidi, E., Liljeback, P., Pettersen, K.Y., Gravdahl, J.T., 2017. Integral line-of-sight guidance for path following control of underwater snake robots: theory and experiments. *IEEE Trans. Robot.* 33 (3), 610–628.
- Klebert, P., Patursson, Ø., Endresen, P.C., Rundtop, P., Birkevold, J., Rasmussen, H.W., 2015. Three-dimensional deformation of a large circular flexible sea cage in high currents: field experiment and modeling. *Ocean Eng.* 104, 511–520.
- Klebert, P., Su, B., 2020. Turbulence and flow field alterations inside a fish sea cage and its wake. *Appl. Ocean Res.* 98 (2020), 102113.
- Kristiansen, T., Faltinsen, O.M., 2012. Modelling of current loads on aquaculture net cages. *J. Fluid Struct.* 34, 218–235.
- Kristiansen, T., Faltinsen, O.M., 2015. Experimental and numerical study of an aquaculture net cage with floater in waves and current. *J. Fluid Struct.* 54, 1–26.
- Lader, P.F., Enerhaug, B., Fredheim, A., Krokstad, J.R., 2003. Modelling of 3D net structures exposed to waves and current. In: Eatock Taylor, R. (Ed.), 3rd International Conference on Hydroelasticity in Marine Technology. Department of Engineering Science, The University of Oxford, Oxford, UK.
- Lader, P.F., Dempster, T., Fredheim, A., Jensen, Ø., 2008. Current induced net deformations in full-scale sea-cages for Atlantic salmon (*Salmo salar*). *Aquacult. Eng.* 38, 52–65.
- Loaland, G., 1991. Current Forces on and Flow through Fish Farms. PhD Thesis. Norwegian University of Science and Technology (NTNU), Trondheim, Norway.
- Milne, P.H., 1983. Underwater Acoustic Positioning Systems. Gulf Publishing.
- Moe-Føre, H., Lader, P.F., Lien, E., Hopperstad, O.S., 2016. Structural response of high solidity net cage models in uniform flow. *J. Fluid Struct.* 65, 180–195.
- Reite, K.J., Føre, M., Aarsæther, K.G., Jensen, J., Rundtop, P., Kyllingstad, L.T., Endresen, P.C., Kristiansen, D., Johansen, V., Fredheim, A., 2014. FhSim - time domain simulation of marine systems. Proceedings of the ASME 2014 33rd International Conference on Ocean, Offshore and Arctic Engineering.
- Remen, M., Solstrom, F., Bui, S., Klebert, P., Vgseth, T., Solstrom, D., Hvas, M., Oppedal, F., 2016. Critical swimming speed in groups of atlantic salmon *salmo salar*. *Aquaculture Environment Interactions* 8, 659–664.
- Rohmer, D., Hahmann, S., Cani, M.P., 2009. Exact volume preserving skinning with shape control. *Proceedings of the ACM SIGGRAPH/Eurographics Symposium on Computer Animation* 83–92.
- Rundtop, P., Frank, K., 2016. Experimental evaluation of hydroacoustic instruments for ROV navigation along aquaculture net pens. *Aquacult. Eng.* 74, 143–156.
- Shen, Y.G., 2018. Operational Limits for Floating-Collar Fish Farms in Waves and Current, without and with Well-Boat Presence. PhD Thesis. Norwegian University of Science and Technology (NTNU), Trondheim, Norway.
- Su, B., Reite, K.J., Føre, M., Aarsæther, K.G., Alver, M.O., Endresen, P.C., Kristiansen, D., Haugen, J., Caharija, W., Tsarau, A., 2019. A multipurpose framework for modelling and simulation of marine aquaculture systems. *Proceedings of the ASME 2019 38th International Conference on Ocean, Offshore and Arctic Engineering*.
- Tang, M.F., Xu, T.J., Dong, G.H., Zhao, Y.P., Guo, W.J., 2017. Numerical simulation of the effects of fish behavior on flow dynamics around net cage. *Appl. Ocean Res.* 64, 258–280.
- Tsukrov, I., Eroshkin, O., Fredriksson, D., Swift, M.R., Celikkol, B., 2003. Finite element modelling of net panels using a consistent net element. *Ocean Eng.* 30 (2), 251–270.
- Turnbull, J., Bell, A., Adams, C., Bron, J., Huntingford, F., 2005. Stocking density and welfare of cage farmed Atlantic salmon: application of a multivariate analysis. *Aquaculture* 243, 121–132.
- Yao, Y., Chen, Y., Zhou, H., Yang, H., 2016. Numerical modeling of current loads on a net cage considering fluid–structure interaction. *J. Fluid Struct.* 62, 350–366.
- Zhao, Y.P., Li, Y.C., Dong, G.H., Gui, F.K., Teng, B., 2007. A numerical study on dynamic properties of the gravity cage in combined wave-current flow. *Ocean Eng.* 34 (17–18), 2350–2363.
- Zhao, Y.P., Bi, C.W., Dong, G.H., Gui, F.K., Cui, Y., Xu, T.J., 2013. Numerical simulation of the flow field inside and around gravity cages. *Aquacult. Eng.* 52, 1–13.